Topics in Catalysis (2023) 66:1102–1119
https://doi.org/10.1007/s11244-023-01849-w

ORIGINAL PAPER

Advanced Kinetic and Titration Strategies for Assessing the Intrinsic Kinetics on Oxide and Sulfide Catalysts

Guangming Cai[1] · William T. Broomhead[1] · Ya-Huei Cathy Chin[1] · Haiting Cai[1,2]

Accepted: 1 July 2023 / Published online: 1 September 2023

Abstract

Found on the surfaces of transition metal oxides or sulfides are metal cations and oxygen or sulfur anions (M^{n+}-O^{2-} or M^{n+}-S^{2-}) with diverse catalytic functions as redox sites (M^{n+}-$O^{2-} \rightarrow$ M-□), Brønsted acid sites (M-OH), and Lewis acid–base sites ($M^{\delta+}$-O^{2-}). These active site pairs often work together in catalyzing the chemical transformation in cascade reactions. This article describes several experimental strategies, combining kinetic and titration methods, to decouple the effects of surface site occupation on turnover rates, identify the kinetic bottlenecks, remove the effects arising from deactivation, as well as elucidate the potential participation of multiple types of active sites. Using a correlative approach in connecting the rate dependencies and titration studies, one could pinpoint the key factors that contribute to the rates and interpret the measured rates in terms of molecular events on the surfaces.

Keywords Kinetics · Metal oxides · Metal sulfides · Active site titration · Competitive reactions

1 Introduction

Transition metal oxides and sulfides are important classes of catalysts for a variety of petro-processing and chemical conversion technologies [1–6], in hydrotreatments that remove organo-sulfur and -nitrogen in aromatic heterocycles [7–9], in hydrodeoxygenation that remove oxygen heteroatoms in biomass derived oxygenates [7], and in cascade synthesis of value-added products [10, 11], where the latter often requires different types of active sites, each with its respective catalytic functionality. Scheme 1 depicts the different types of active sites on oxide (1a) and sulfide (1b) surfaces. Found on these surfaces are metal cations (M^{n+}) and oxygen/sulfur anions (O^{2-}/S^{2-}); these cations and anions would exhibit different chemical and electronic properties, depending on the exposed facets and specific termination, and even for ions on the same surface, their properties would vary with their immediate coordination environment. These exposed ions and their vacancies would acquire diverse catalytic roles, as single ions, site pairs, or vacancy sites in catalytic sojourns [1–3].

On metal oxides, lattice cation–anion site pairs (M^{n+}-O^{2-}) are effective for interacting with the C–H bond in reacting precursors, e.g., that in alkanes (V–O [12], Fe–O [13], Co–O [14, 15], Ni–O [13, 15], Ga-O [16], Zn–O [17], Mo–O [18], and In-O[14, 19]) and in alkanols (V–O[20, 21] and Mo–O[18]). In the classical Mars-van Krevelen mechanism, the lattice O^{2-} anion is removed in a reduction half cycle, during which the oxides undergo reduction to a lower oxidation state and a lattice oxygen vacancy □ is formed. The lattice O^{2-} anion is regenerated by O_2 dissociation in the oxidation half cycle, returning the oxide to its initial state and completing the redox cycle [22–24]. In addition to the lattice cation–anion pairs, coordinatively-unsaturated metal cationic sites ($M^{\delta+}$, e.g., Al^{3+},[25] Ga^{3+},[26] Ti^{4+},[27] and Sn^{4+} [28]) could act as Lewis acid centers, catalyzing dehydration reactions, e.g., alkanols inter- and intra-molecular dehydration [29–32]. Last, found binding to the oxygen anions are Brønsted acidic protons, and these protons are

✉ Ya-Huei Cathy Chin
cathy.chin@utoronto.ca

✉ Haiting Cai
caihaiting@zjut.edu.cn

[1] Department of Chemical Engineering and Applied Chemistry, University of Toronto, Toronto, ON M5S 3E5, Canada

[2] Institute of Industrial Catalysis, State Key Laboratory of Green Chemistry Synthesis Technology, College of Chemical Engineering, Zhejiang University of Technology, Hangzhou, Zhejiang 310014, China

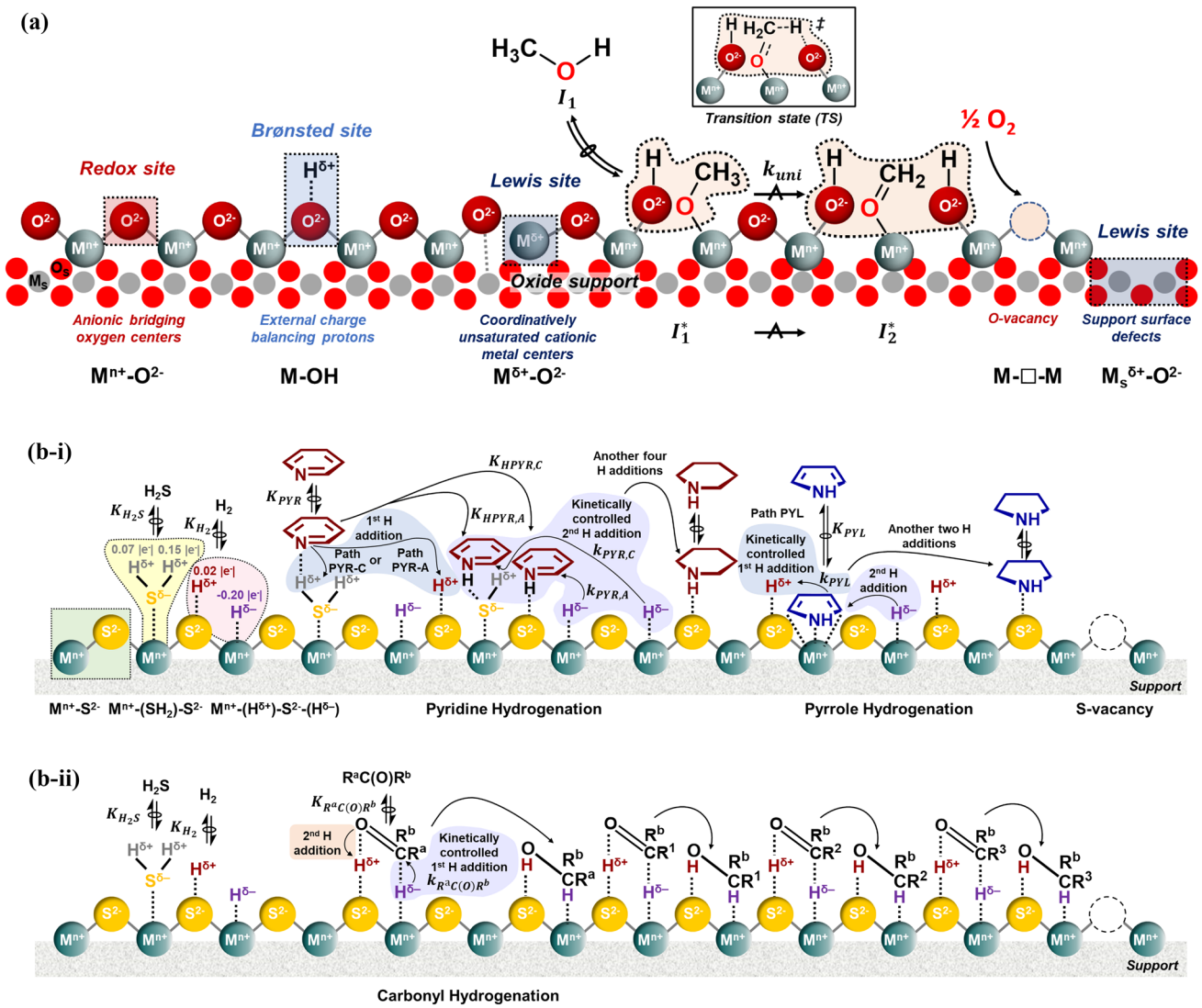

Scheme 1 Illustrations of **a** supported metal oxides, including their redox (red, M^{n+}-O^{2-}), Brønsted acid (light blue, M-OH), Lewis acid (dark blue, $M^{\delta+}$-O^{2-}) sites, O-vacancy (M-□-M), and the Lewis acid site on the uncovered oxide support ($M_s^{\delta+}$-O^{2-}), as well as surface intermediates of dissociative adsorbed methanol (I_1^*), formed formaldehyde (I_2^*) in the kinetically relevant C–H scission step (⇀A↽), and the transition state structure (TS) in methanol oxidative dehydrogenation (ODH), and **b** supported metal sulfides, where reactive hydrogen atoms acquire distinct proton [$H^{\delta+}$ in M^{n+}-($H^{\delta-}$)-L^{m-}-($H^{\delta+}$), red; $H^{\delta+}$ in M^{n+}-(SH_2)-L^{m-}, gray)] or hydride [$H^{\delta-}$ in M^{n+}-($H^{\delta-}$)-L^{m-}-($H^{\delta+}$), purple] properties, and demonstrate different catalytic roles in hydrogen addition events of **b–i** pyridine and pyrrole hydrogenation, and **b–ii** carbonyl hydrogenation. The results of **b** are from Refs. [7, 8]

known to catalyze alkanol C–O bond formation[25, 33, 34] as well as alkane isomerization [33, 35, 36].

Similarly, found on transition metal sulfides are lattice M^{n+} cation-S^{2-} anion pairs (M^{n+}-S^{2-}). These cation–anion pairs could interact with and polarize H_2S and assist with its dissociative adsorption that replenishes the lattice S^{2-} anions [37, 38], similar to what described above for the case of oxides. Here, the removal of lattice S^{2-} anions, typically occurring on the edges of the sulfide catalysts (e.g., $CoMoS_x$[39, 40] and MoS_x[41]), leads to the formation of coordinatively unsaturated sites that promote the scission of C-S bond in hydrodesulfurization. Alternatively, H_2S may also adsorb molecularly on the M^{n+} cation-S^{2-} anion pairs of the S-deficient metal sulfide surfaces (e.g., RuS_x[8]). The sulfide surfaces interact with the heterocycles mainly through van der Waals interactions, [42] due partly to the large footprint of the heterocycles. In addition, the binding of reactive hydrogen species on lattice M^{n+} cation-S^{2-} anion pairs can further polarize the hydrogen, thus the hydrogen on sulfide acquires hydride or proton functionality in hydrogen attack catalysis [8].

These diverse types of active sites have made oxides and sulfides versatile catalysts for catalyzing complex cascade reactions requiring multiple types of sites [1–9]. To date, straightforward experimental methods for quantitatively counting each type of site (redox, Brønsted, Lewis) are, however, limited. Additionally, it has been well recognized that for the various types of sites, their surface densities, thermochemical properties, and in turn kinetic properties vary with the operating conditions and with each other, [43, 44] e.g., creating an oxygen vacancy (M-□) on the oxide surfaces would affect the Lewis acidity of the vicinal $M^{\delta+}$ cation [45]. This structural complexity has precluded an unambiguous comparison on the active site densities, their relative abundance, and their individual turnovers among the various oxides/sulfides, making it difficult to establish the structure–reactivity relationships.

The general turnover rate expressions for reactions with an uni- or bi-molecular kinetically relevant step ($r_{uni,\sigma=1}$, $r_{bi,\sigma=2}$, or $r_{bi,\sigma=1}$ per site, where subscript *uni* or *bi* denotes uni- or bi-molecular elementary reaction, respectively, and subscript $\sigma = 1$ or $\sigma = 2$ represents the number of active sites involved in the kinetically relevant step) are:

$$\text{Type} - \text{I}: \; r_{uni,\sigma=1} = \frac{k_{uni,\sigma=1}\left[M^{n+} - \left(I_a\right) - L^{m-}\right]}{\left[T_{M-L}\right]} \tag{1}$$

$$\text{Type} - \text{II}: \; r_{bi,\sigma=2} = \frac{k_{bi,\sigma=2}\left[M^{n+} - \left(I_b\right) - L^{m-}\right]\left[M^{n+} - \left(I_c\right) - L^{m-}\right]}{[T_{M-L}]^2} \tag{2}$$

$$\text{Type} - \text{III}: \; r_{bi,\sigma=1} = \frac{k_{bi,\sigma=1}\left[M^{n+} - \left(I_d\right) - L^{m-}\right]\left[I_E\right]}{\left[T_{M-L}\right]} \tag{3}$$

where $k_{uni,\sigma=1}$, $k_{bi,\sigma=2}$, and $k_{bi,\sigma=1}$ denote elementary rate constants for the respective kinetically relevant step; the symbol M^{n+}-L^{m-} denotes the exposed active site pair of M^{n+} cation ($M^{n+} = Mo^{6+}$, Ru^{4+}, etc.) and L^{m-} ligand ($L^{m-} = O^{2-}$, S^{2-}, etc.); $[I_\Omega]$ represents the partial pressure of reactant I_Ω (subscript Ω = A, B, C, D, or E); M^{n+}-(I_ω)-L^{m-} refers to the adsorbed precursor (subscript ω = a, b, c, or d), derived from reactant I_Ω, for the kinetically relevant step. $[T_{M\text{-}L}]$ refers to the sum of the fractional coverages of all adsorbates and the unoccupied site:

$$\left[T_{M-L}\right] = \left[M^{n+} - L^{m-}\right] + \left[M^{n+} - \left(I_\omega\right) - L^{m-}\right] + \ldots \tag{4}$$

These expressions are expanded using pseudo steady-state treatments or quasi-equilibrium expressions and described in terms of the thermodynamic activity of the respective species in the gas or liquid phase (denoted by square brackets), and for the case of reaction at gas–solid interfaces, in terms of partial pressure of I_Ω. Here, $k_{eff,uni,\sigma=1}$, $k_{eff,bi,\sigma=2}$, and $k_{eff,bi,\sigma=1}$ are the effective rate coefficients, accounting for the quasi-equilibrated steps required for the formation of the reactive precursors, M^{n+}-(I_ω)-L^{m-}, occurred before the kinetically relevant step.

$$\text{Type} - \text{I}: \; r_{uni,\sigma=1} = \frac{k_{eff,uni,\sigma=1}\left[I_A\right]^{q_A}\left[M^{n+} - L^{m-}\right]}{\left[T_{M-L}\right]} \tag{5}$$

$$\text{Type} - \text{II}: \; r_{bi,\sigma=2} = \frac{k_{eff,bi,\sigma=2}\left[I_B\right]^{q_B}\left[I_C\right]^{q_C}\left[M^{n+} - L^{m-}\right]^2}{[T_{M-L}]^2} \tag{6}$$

$$\text{Type} - \text{III}: \; r_{bi,\sigma=1} = \frac{k_{eff,bi,\sigma=1}\left[I_D\right]^{q_D}\left[I_E\right]^{q_E}\left[M^{n+} - L^{m-}\right]}{\left[T_{M-L}\right]} \tag{7}$$

where q_Ω denotes the reaction order of I_Ω in the kinetically relevant step.

This perspective article describes a variety of experimental strategies towards analyzing complex reactions on oxide and sulfide surfaces, assembled in the forms of several case studies, on oxides (Sect. 2) and sulfides (Sect. 3). For the case of oxides, the various reactions in the methanol-O_2 reaction network that leads to the formation of larger oxygenates, catalyzed by acid and redox sites, are examined with strategies accounting for active site losses during steady-state reactions, strategies of introducing a titrant to probe the change in rates in response to changing site density and proximity, strategies to altering the oxygen contents in oxides, and strategies to probe the kinetic significance of each type of sites. For the sulfide surfaces, the various terms in the rate expressions of hydrogenation chemistry of heterocycles and carbonyls are extracted with experimental strategies, through controlling and setting the constant sulfur chemical potentials and therefore the number of active site pairs, in particular, the surface abundance of the various reactive hydrogen species, and through removing the effects of coverages in competitive reactions using a reference compound. These suites of experimental techniques allow probing the number of various types of active sites as well as their catalytic turnovers. Together, they would allow us to interpret the measured catalytic rates with molecular level insights and to connect the findings to those derived from computational studies.

2 Strategies to Interrogate Intrinsic Kinetics and Decipher Site Functionalities on Oxide Surfaces

Scheme 2 shows the full reaction network in CH_3OH-O_2 reactions on metal oxides, typically as nanometer sized redox-active oxide domains dispersed on another oxide of

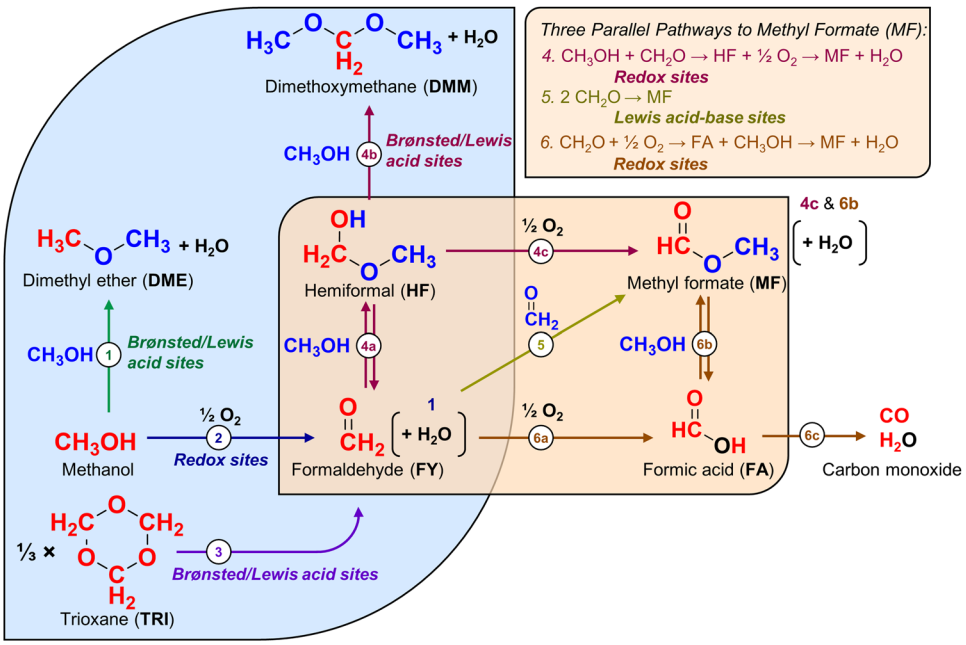

Scheme 2 Reaction network for CH_3OH–O_2–CH_2O reactions on multifunctional metal oxide catalysts. Reactions highlighted in blue are covered in Sects. 2.1–2.2, and reactions highlighted in orange regarding three concomitant pathways that produce methyl formate are covered in Sect. 2.3

high surface area, e.g., VO_x/TiO_2 [21], MoO_x/TiO_2 [46], and $H_3PMo_{12}O_{40}/SiO_2$ [47], with coexisting redox, Brønsted, and/or Lewis acidic functions, shown in Scheme 1a. These oxides catalyze two primary pathways (1 and 2) of (i) methanol intermolecular dehydration (DEH) to form dimethyl ether (DME, CH_3OCH_3) via a kinetically relevant C–O bond formation step (Pathway 1) [34], catalyzed by Brønsted and/or Lewis sites, and (ii) methanol oxidative dehydrogenation (ODH) to form formaldehyde (FY, HCHO) and water via a kinetically relevant C–H bond activation step (Pathway 2) [22, 48], in a classical Mars-van Krevelen mechanism catalyzed by the redox active O-atom. The formaldehyde could undergo acid catalyzed secondary reactions to produce dimethoxymethane (DMM, $CH_3OCH_2OCH_3$) via two consecutive C–O bond formation steps, first that forms hemiformal (HF, CH_3OCH_2OH, Pathway 4a) and second that converts the hemiformal by reacting with another methanol to produce dimethoxymethane (Pathway 4b). The formaldehyde and hemiformal are both precursors for methyl formate (MF, $HCOOCH_3$) that could be produced via three parallel secondary pathways (Pathways 4c, 5, and 6a/6b) of (i) oxidative dehydrogenation of hemiformal occurring on redox sites (Pathway 4c) [49], (ii) Tishchenko reaction of two formaldehydes occurring on Lewis acid sites (Pathway 5) [50, 51], and (iii) oxidation of formaldehyde to form formic acid (FA, HCOOH) occurring on redox sites (Pathway 6a), followed by the reaction of formic acid and methanol occurring on acid sites (Pathway 6b) [52]. The formed formic acid can also undergo sequential oxidation on the redox sites, forming CO_x and water (Pathway 6c).

2.1 Case Study I: Measurements of Intrinsic Kinetics Accounting for Gradual Loss of Active Sites

In Eqns. 5, 6 and 7, the surface concentration of the total active sites ($[T_{M-L}]$) may decrease with time-on-stream (t) due to irreversible site occupation by products or poisons. Illustrated here is an example for the synthesis of dimethoxymethane, a fuel additive, from methanol and trioxane (TRI, $C_3H_6O_3$, a cyclic precursor of formaldehyde) on Keggin-type phosphotungstic acid polyoxometalate (POM) clusters ($H_3PW_{12}O_{40}$, hereinafter denoted as H_3PW), which contain only Brønsted sites (M-OH). In this case, only Pathways 1, 3, 4a, and 4b (Scheme 2) prevail; the decomposition of trioxane on Brønsted sites in Pathway 3 produces three formaldehyde units that enter the reaction network described above (Pathways 4a and 4b) in Scheme 2 to react with a stoichiometric amount of methanol, forming three dimethoxymethane molecules. Among Pathways 3, 4a, and 4b, trioxane decomposition (*dec*) limits the overall reactions and the sequential formaldehyde-methanol reactions are reported as kinetically irrelevant [53, 54]. Based on reaction stoichiometry, the formation rate of dimethoxymethane [r'_{DMM}, superscript $'$ denotes units of μmol $(g_{cat}\ h)^{-1}$] thus equals:

$$r'_{DMM}\left[\frac{\mu mol}{g_{cat}h}\right] = 3r'_{TRI,dec} \tag{8}$$

Figure 1a shows the rates of dimethoxymethane formation ($r'_{DMM,t}$) as a function of time-on-stream (t) at 338 K, under different trioxane and methanol partial pressures. The rate measurements were carried out first in the reference condition

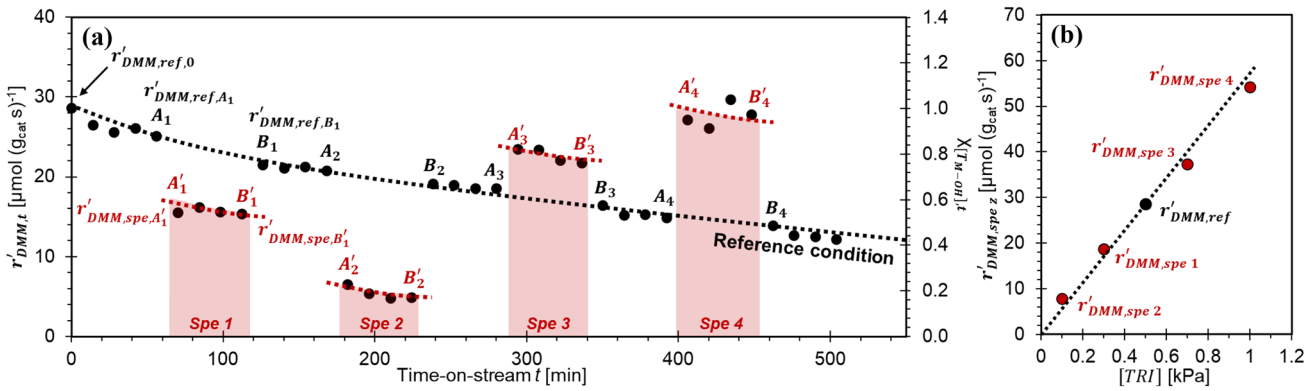

Fig. 1 **a** Measured DMM formation rates $r'_{DMM,t}$ during kinetic measurements with methanol-trioxane catalysis as an example, illustrating the method to obtain the intrinsic rates with a reference reaction condition at various specific conditions [*Spe z*, $z=1$–4. $z=1$, $[TRI]=$ 0.3 kPa; $z=2$, $[TRI]=$ 0.1 kPa; $z=3$, $[TRI]=$ 0.7 kPa; $z=4$, $[TRI]=$ 1.0 kPa. 2.0 kPa methanol, 0.5 kPa trioxane and 2.0 kPa methanol as a reference condition, Brønsted acidic $H_3PW_{12}O_{40}$ clusters supported on inert high surface area silica (0.14 POM nm^{-2}), 4.1 cm^3 (μmol$_{POM}$ s)$^{-1}$, 338 K] alongside the fraction of total Brønsted sites ($\chi_{[T_{M-OH}],t}$) during reactions. **b** Trioxane dependence for the intrinsic DMM formation rates ($r'_{DMM,spez}$) at a constant methanol pressure (2.0 kPa) resulting from the method shown in **a**

(e.g., $[TRI]_{ref}=0.5$ kPa, $\left[CH_3OH\right]_{ref}=2.0$ kPa) for approximately two hours, after which the feed compositions were rapidly switched from the reference condition to a specific condition (denoted as *Spe 1*), which corresponds to point A_1 to A'_1 on the figure. After approximately an hour, the feed compositions were switched from the specific condition (*Spe 1*) back to the reference condition again (B'_1 to B_1) to acquire the rate data under reference conditions. After about an hour, the feed compositions were changed again to another specific condition (*Spe 2*), and the switching of the feed compositions was repeated several times with different sets of specific condition (*Spes 3* and *4*). As shown in Fig. 1a, the rates $r'_{DMM,t}$ decreased by 60% over the course of the reactions, when comparing the rate values measured at the initial time ($t\approx 0$) and those at the end of the kinetic experiments (500 min) at the reference condition. This decrease is caused by one or more of formaldehyde polymerization, coking, and the formation of long chain polyoxymethylene dimethyl ethers ($CH_3O(CH_2O)_nCH_3$, $n>1$), as these species would occupy and block the Brønsted sites, as previously explored and established with thermogravimetric and mass spectrometric analysis in methanol-formaldehyde reactions [55].

Combining the relationships between dimethoxymethane formation and kinetically relevant trioxane decomposition (Eq. 8) with the rate expression in a unimolecular kinetically relevant reaction (Type-I) displayed in Eq. 5, dimethoxymethane formation rate (r'_{DMM}) can be expressed as:

$$\begin{aligned} r'_{DMM} &= 3r_{TRI,dec}\left[T_{M-OH}\right] \\ &= 3k_{eff,TRI,dec}[M-OH][TRI] \\ &= 3k_{eff,TRI,dec}\theta_{M-OH}\left[T_{M-OH}\right][TRI] \end{aligned} \tag{9}$$

where $k_{eff,TRI,dec}$ refers to the effective trioxane decomposition rate constant on Brønsted sites; $\left[T_{M-OH}\right]$ and $[M-OH]$ refer to the densities of total and unoccupied Brønsted sites during reaction, respectively; and θ_{M-OH} refers to the coverage of free Brønsted sites ($\theta_{M-OH}=[M-OH]\left(\left[T_{M-OH}\right]\right)^{-1}$). As the densities of total Brønsted site ($\left[T_{M-OH}\right]$) decrease, the rate values acquire an additional dependence on the time-on-stream, t. The following experimental procedures account for the time dependent Brønsted site density $\left[T_{M-OH}\right]_t$ in treating the rate data.

(1) At initial time ($t\approx 0$) and any time-on-stream t, the dimethoxymethane formation rates ($r'_{DMM,ref,0}$ and $r'_{DMM,ref,t}$) at a reference reaction condition (*ref*, e.g., $[TRI]_{ref}=0.5$ kPa, $\left[CH_3OH\right]_{ref}=2.0$ kPa), based on Eq. 9, equal Eqns. 10 and 11, respectively:

$$r'_{DMM,ref,0}=3k_{eff,TRI,dec}\theta_{M-OH}\left[T_{M-OH}\right]_0[TRI]_{ref} \tag{10}$$

$$r'_{DMM,ref,t}=3k_{eff,TRI,dec}\theta_{M-OH}\left[T_{M-OH}\right]_t[TRI]_{ref} \tag{11}$$

The fraction of total Brønsted sites on POM clusters ($\chi_{[T_{M-OH}],t}$) can be defined and quantified based on the rate ratio of dimethoxymethane formation at time t ($r'_{DMM,ref,t}$) to that at the initial time ($t=0$, $r'_{DMM,ref,0}$) at the reference reaction condition:

$$\chi_{[T_{M-OH}],t}=\frac{\left[T_{M-OH}\right]_t}{\left[T_{M-OH}\right]_0}=\frac{r'_{DMM,ref,t}}{r'_{DMM,ref,0}} \tag{12}$$

$\chi_{[T_{M-OH}],t}$ expresses the fraction of the total Brønsted sites remaining during deactivation and is shown in Fig. 1a. This treatment assumes that the Brønsted sites are uniform in acid strength and exhibit identical turnover rates per site (i.e., constant $k_{eff,TRI,dec}\theta_{M-OH}$ at the same reaction condition), and the reaction involves isolated Brønsted sites and not Brønsted site pairs (i.e., a unimolecular reaction on one active site, Eq. 5).

(2) During kinetic measurements, e.g., in methanol-trioxane reactions, dimethoxymethane formation rates immediately before (timeA_z) and after (timeB_z) the switching from the reference condition to specific condition are designated as r'_{DMM,ref,A_z} andr'_{DMM,ref,B_z}, respectively, which reflect dimethoxymethane formation rates under the reference condition before and after the reactions under specific condition *Spe z*, as indicated in Fig. 1a. During reactions under the specific condition *Spe z* (shaded area in red in Fig. 1a), dimethoxymethane formation rates in the beginning (timeA'_z) and at the end (timeB'_z) of the measurement are designated as r'_{DMM,spe,A'_z} and r'_{DMM,spe,B'_z}, respectively.

The method described above assumes that the fraction of total Brønsted sites remains unchanged over a short period of time (~ 14 min, i.e., the time requires for rate data sampling), i.e., the time period from A_z to A'_z and from B'_z to B_z:

$$\chi_{[T_{M-OH}],A'_z} = \chi_{[T_{M-OH}],A_z} \tag{13}$$

$$\chi_{[T_{M-OH}],B'_z} = \chi_{[T_{M-OH}],B_z} \tag{14}$$

Therefore, the average fraction of total Brønsted sites at *Spe z* is:

$$\chi_{[T_{M-OH}],spez} = \frac{\chi_{[T_{M-OH}],A_z} + \chi_{[T_{M-OH}],B_z}}{2} = \frac{r'_{DMM,ref,A_z} + r'_{DMM,ref,B_z}}{2r'_{DMM,ref,0}} \tag{15}$$

Finally, the extrapolated dimethoxymethane formation rates at the specific condition *Spe z* ($r'_{DMM,spez}$) after considering site loss is:

$$r'_{DMM,spez} = \frac{r'_{DMM,spe,A'_z} + r'_{DMM,spe,B'_z}}{2\chi_{[T_{M-OH}],spez}} = \frac{\left(r'_{DMM,spe,A'_z} + r'_{DMM,spe,B'_z}\right) \times r'_{DMM,ref,0}}{r'_{DMM,ref,A_z} + r'_{DMM,ref,B_z}} \tag{16}$$

Figure 1b shows the first-order dependence of dimethoxymethane formation rate $r'_{DMM,spez}$ to trioxane pressure in methanol-trioxane reactions with the measured kinetic data (r'_{DMM,spe,A'_k} and r'_{DMM,spe,B'_k}) corrected by Eq. 16, after accounting for the site losses during the kinetic experiments. This correction eliminates the potential misinterpretations from the measured reaction rates without considering site deactivation. Similarly, for redox catalyzed reactions (M^{n+}-O^{2-}), such as C_2H_6–CO_2 reactions to produce C_2H_4 on molybdenum oxides supported on inert alumina (MoO_x/Al_2O_3), the product selectivity to various products (C_2H_6, CH_4, and CO) did not change along with time-on-stream despite C_2H_6 conversion continued to decrease, indicating that only the number of active sites decays, while their reactivity (per active site) does not change [56]. Thus, in redox catalysis the prerequisites are still fulfilled and this strategy, reflected in Eqns. 12–16, can be used to account for redox site deactivation.

2.2 Case Study II: Interrogating the Acid and Redox Connectivity, in Thermochemical and Kinetic Properties, on Bifunctional Metal Oxides

CH_3OH-O_2 reactions depicted in Scheme 2 could also occur on other classes of reducible oxides (VO_x/TiO_2 [21, 57], ReO_2/M_sO_2 (M_s = Sn, Zr, Ti, or Si) [58], etc.) that exhibit both redox and acid functionalities. These oxides are structurally more complex than polyoxometalate clusters used in Sect. 2.1 because they are dispersed on a support with varying domain sizes. For this reason, not only the densities of redox and acid sites, but their electronic properties, i.e., HOMO–LUMO bandgap energies, and kinetic properties differ. Using a bimetallic $FeMoO_x$ oxide as the example, we describe the experimental strategies, in the following two sub-sections, to unravel the connectivity between the acid and redox catalyzed reaction rates and the effects of oxygen contents on the turnovers of these sites, respectively.

2.2.1 Correlations Between Acid and Redox Sites on SiO_2-Supported $FeMoO_x$

Bimetallic $FeMoO_x$ oxides supported on inert silica ($FeMoO_x/SiO_2$; Fe-to-Mo atomic ratio of 1/3) contain both Lewis acid ($M^{\delta+}$-O^{2-}) and redox (M^{n+}-O^{2-}) sites, as confirmed from pyridine absorption infrared spectroscopy and inferred from the product distributions. The connectivity between these two types of sites, in terms of their catalytic turnovers, is probed from the changes in the respective catalytic turnovers—Lewis sites catalyze the primary methanol intermolecular dehydration [DEH, Pathway 1 in Scheme 2, r'_{DEH}, unit of μmol $(g_{cat}\ s)^{-1}$] that proceeds via a bimolecular elementary reaction (Type-III) and redox sites catalyze the primary methanol oxidative dehydrogenation (ODH, Pathway 2 in Scheme 2, r'_{ODH}) that proceeds via a unimolecular elementary reaction (Type-I)—in response

to site occupation by basic pyridine titrant. Based on their respective turnover rate expression in Eqns. 7 and 5, the rate expressions for methanol DEH (r'_{DEH}) and ODH (r'_{ODH}) are given below:

$$r'_{DEH} = k_{eff,DEH}\left[M^{\delta+} - O^{2-}\right]\left[CH_3OH\right]^2 = k_{eff,DEH}\theta_{M^{\delta+}-O^{2-}}\left[T_{M^{\delta+}-O^{2-}}\right]\left[CH_3OH\right]^2 \quad (17)$$

$$r'_{ODH} = k_{eff,ODH}\left[M^{n+} - O^{2-}\right]\left[CH_3OH\right] = k_{eff,ODH}\theta_{M^{n+}-O^{2-}}\left[T_{M^{n+}-O^{2-}}\right]\left[CH_3OH\right] \quad (18)$$

where $k_{eff,DEH}$ and $k_{eff,ODH}$ refer to the effective rate constants for methanol DEH and ODH, respectively; $\left[M^{\delta+} - O^{2-}\right]$ and $\left[M^{n+} - O^{2-}\right]$ refer to the densities of unoccupied Lewis sites and redox sites, respectively, $\theta_{M^{\delta+}-O^{2-}}$ and $\theta_{M^{n+}-O^{2-}}$ refer to the coverages of unoccupied Lewis sites and redox sites during CH_3OH-O_2 reactions, respectively, and $\left[CH_3OH\right]$ refers to the partial pressure of methanol.

Figure 2a shows the suppression in the reaction rates of both methanol DEH (r'_{DEH}) and ODH (r'_{ODH}) during pyridine titration in CH_3OH-O_2 reactions at 453 K. At steady-state, both methanol DEH and ODH did not change with time-on-stream, indicating that the coverages and concentrations of Lewis sites and redox sites, in terms $\theta_{M^{\delta+}-O^{2-}}$ and $\theta_{M^{n+}-O^{2-}}$ as well as $\left[T_{M^{\delta+}-O^{2-}}\right]$ and $\left[T_{M^{n+}-O^{2-}}\right]$ in Eqns. 17 and 18, respectively, remain essentially constant. Introduction of pyridine led to pyridine adsorption on Lewis sites, thus the total Lewis sites ($\left[T_{M^{\delta+}-O^{2-}}\right]$) available for catalysis decrease, leading the methanol DEH rates to concomitantly decrease to ~ 10% of its initial value (Fig. 2a). The methanol ODH rates that occur at redox sites ($\left[T_{M^{n+}-O^{2-}}\right]$) also decreased to similar extent; in fact, the DEH and ODH rates appear to correlate with each other during the entire duration of in situ pyridine titration, shown in Fig. 2b, indicating these two types of sites are correlated. The decrease in methanol ODH rates due to Lewis sites being occupied by pyridine can be explained by:

(i) Redox site occlusion, where the term $\left[T_{M^{n+}-O^{2-}}\right]$ in Eq. 18 decreases with pyridine adsorption because the steric hindrance exerted by vicinal pyridine may prevent methanol molecules from accessing redox sites, or

(ii) Manipulation of intrinsic redox site reactivity, where the term $k_{eff,ODH}$ in Eq. 18 decreases with pyridine adsorption because charge transfer from the electron lone pair in the N-atom of pyridine to Lewis sites may change the electronic and thermochemical properties of the redox sites [22].

We note that one of the strategies to probe the above two possibilities on the ODH rate suppression is to alter the size of the basic titrant, e.g., comparing pyridine (5.3 Å) to 3,5-di-methylpyridine (5.2 Å), 2,6,-di-methylpyridine (5.9 Å), and 2,6,-di-ethylpyridine (6.3 Å) [59]. As the size of the basic titrant increases, the inhibitory effects on methanol ODH would become stronger when steric hindrance of the titrants is the key factor. Otherwise, the modification of thermodynamic properties of redox sites is the key factor.

2.2.2 Catalytic Consequences of Bulk $FeMoO_x$ Oxygen Contents on ODH and DEH Rates

The oxygen content x in $FeMoO_x$ oxides reflects the average oxidation state of the M^{n+} cation and the extent of reduction, among other properties; it also reflects the differential oxygen binding energies and the related oxygen vacancy formation energies, i.e., the energies required to extract an additional oxygen atom from the $FeMoO_x$ oxides ($FeMoO_x \rightarrow FeMoO_{x-1} + O_{atom}$, ΔH_f^{Ov}). The abstraction of oxygen (or reduction of M^{n+} cation) modifies the electronic properties of M^{n+} cation and changes the electronegativity [through the work function (φ) or electron chemical potential (μ_e)] of the metal centers and in turn their Lewis acidity [45, 60].

Figures 3a, b show the effects of instantaneous oxygen contents on the ODH and DEH turnovers on bulk $FeMoO_x$ oxides (Fe-to-Mo atomic ratio of 1/3) obtained from measuring the turnovers in the following sequence: (i) steady-state CH_3OH-O_2 feed (Period I), (ii) the removal of O_2 from the feed (Period II), and (iii) re-introducing O_2 to the feed (Period III) at 423 K. During steady-state CH_3OH-O_2 catalysis, the $FeMoO_x$ oxide catalysts were fully oxidized, as both methanol ODH and DEH reactions were zero order to oxygen. In this case, methanol C–H bond activation in ODH and C–O bond formation in DEH are their respective sole rate limiting steps, and the species independent

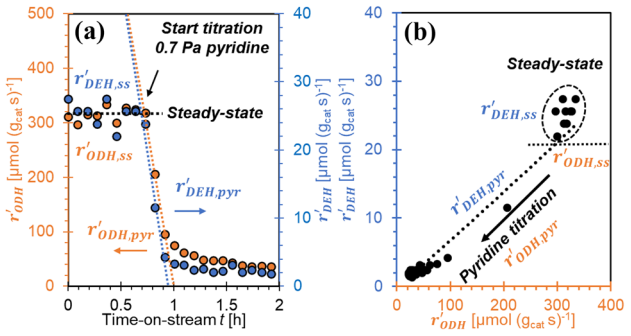

Fig. 2 **a** Methanol oxidative dehydrogenation (ODH) and dehydration (DEH) rates during steady-state (r'_{ODH} and r'_{DEH}) and during pyridine titration ($r'_{ODH,pyr}$ and $r'_{DEH,pyr}$) in CH_3OH-O_2 catalysis [Fe_2O_3-MoO_3/SiO_2 catalyst (Fe to Mo atomic ratio of 1/3, 13.5 wt% MoO_3 supported on silica), 2.2 kPa CH_3OH and 40 kPa O_2, 606 cm^3 (g_{cat} min)$^{-1}$, 0.014 μmol$_{pyr}$ min^{-1}, 453 K]. **b** Correlations of methanol ODH and methanol DEH reaction rates during pyridine titration in **a**

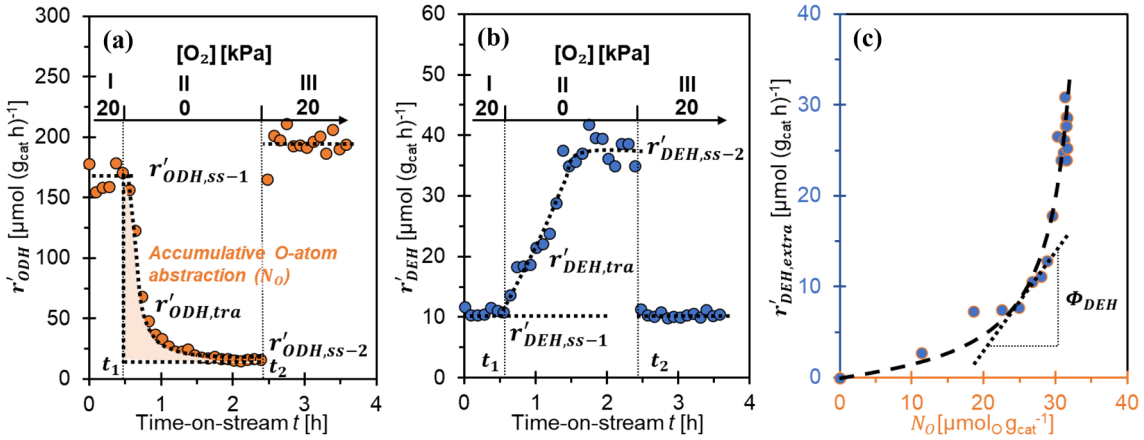

Fig. 3 Transient profiles of **a** methanol ODH (r'_{ODH}) and **b** methanol DEH (r'_{DEH}) in CH_3OH-O_2 reactions (Period I), removal of O_2 from the CH_3OH-O_2 feed (Period II), and recovering of O_2 to the feed (Period III) with two steady-state reaction rates ($r'_{ODH,ss-1}$ and $r'_{ODH,ss-2}$; $r'_{DEH,ss-1}$ and $r'_{DEH,ss-2}$) and their transient rates ($r'_{ODH,tra}$ and $r'_{DEH,tra}$), respectively (bulk $FeMoO_x$ catalyst (Fe to Mo atomic ratio of 1/3), 2.0 kPa CH_3OH, 20→0→20 kPa O_2, 116 cm^3 (g_{cat} min)$^{-1}$, 423 K). **c** Correlations between accumulative lattice oxygen abstraction (N_O) and extra methanol DEH rate ($r'_{DEH,extra}$) defined in Eqns. 20 and 21, and schematic description of the slope of the curve (Φ_{DEH}) defined in Eq. 22

selectivity to DEH was ~ 5%. In Period II, shutting off O_2 (at time-on-stream t_1) led the methanol ODH rate to decrease from $r'_{ODH,ss-1}$ in the steady state with oxygen to a much lower reaction rate $r'_{ODH,ss-2}$ (Fig. 3a). In contrast, the methanol DEH turnovers in the parallel reaction increased from $r'_{DEH,ss-1}$ to $r'_{DEH,ss-2}$ with time-on-stream (Fig. 3b). The reintroduction of O_2 in Period III led both methanol ODH and DEH turnovers to return to their respective values of Period I.

The time-dependent rates in response to the switch from Period I to Period II reflect a change in the oxygen contents ($[T_{M^{n+}-O^{2-}}]$) and/or in the reactivity of redox site ($k_{eff,ODH}$) as the redox oxygen atoms in M^{n+}-O^{2-} are depleted by their ODH reaction with methanol, leaving O-vacancies (M-□-M) that could not be refilled in the absence of O_2. Thus, methanol ODH rate values acquire an additional dependence on the time-on-stream during the transient experiment of Period II (*tra*):

$$r'_{ODH,tra} = k_{eff,ODH,tra,t}\theta_{M^{n+}-O^{2-}}\left[T_{M^{n+}-O^{2-}}\right]_{tra,t}[CH_3OH] \quad (19)$$

The decrease in site density and/or reactivity of the redox site led to the commensurate decrease in methanol ODH rate (Fig. 3a). Since one methanol ODH turnover abstracts one oxygen center, the total oxygen centers (N_O) abstracted during Period II can be evaluated by integrating the difference between the transient ($r'_{ODH,tra}$) and steady-state ($r'_{ODH,ss-2}$) methanol ODH rates from the starting point (t_1) to the end point (t_2) of the transient experiment:

$$N_O\left(\frac{\mu mol_O}{g_{cat}}\right) = \int_{t_1}^{t_2}\left(r'_{ODH,tra} - r'_{ODH,ss-2}\right)dt \quad (20)$$

The increase in methanol DEH rate is caused by one or both of the following reasons: (i) the creation of more acid sites (either Brønsted sites or Lewis sites) due to the formation of oxygen vacancy (M-□-M), thus there is an increase in the site density term $\left[T_{M^{\delta+}-O^{2-}}\right]$ in Eq. 17; and (ii) the increase in Lewis acid strength as oxygen vacancies form, thus the $k_{eff,DEH}$ in Eq. 17 increases. The enhancement of methanol DEH reaction rate ($r'_{DEH,extra}$), originating from catalysts reduction, is defined by the difference between transient methanol DEH rate ($r'_{DEH,tra}$) and the rate in the initial steady-state ($r'_{DEH,ss-1}$):

$$r'_{DEH,extra} = r'_{DEH,tra} - r'_{DEH,ss-1} \quad (21)$$

Figure 3c shows the relationship between the instantaneous abstracted oxygen centers (N_O) and the extra methanol DEH rate ($r'_{DEH,extra}$) during Period II in Figs. 3a, b. The slope of the curve at any amount of abstracted oxygen centers (Φ_{DEH}) is defined as:

$$\Phi_{DEH}\left(\frac{\mu mol_{DEH}}{\mu mol_O h}\right) = \frac{dr'_{DEH,extra}}{dN_O} \quad (22)$$

Φ_{DEH} captures the effects of oxygen abstraction on the modification of acid properties of catalysts. On bulk $FeMoO_x$ oxides, Φ_{DEH} increased with increasing of the amount of abstracted oxygen centers, indicating that the extra methanol DEH rate ($r'_{DEH,extra}$) increased much faster with more oxygen abstracted. These results imply that the modification of acid sites becomes increasingly severe with more oxygen vacancies on the surface.

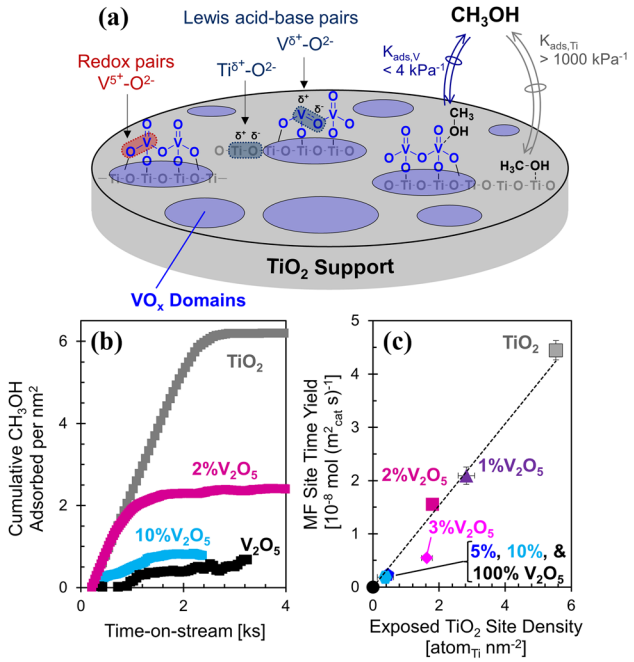

Fig. 4 **a** Schematic of a VO_x/TiO_2 catalyst, illustrating the various types of active sites, including redox (V^{5+}-O^{2-}) and Lewis acid–base ($V^{\delta+}$-O^{2-}) site pairs found on the VO_x moieties as well as Lewis acid–base ($Ti^{\delta+}$-O^{2-}) site pairs on exposed TiO_2; these site pairs catalyze one or more reactions in Pathways 4–6 of Scheme 2. The fraction of the surface comprised of exposed TiO_2 (colored gray) was quantified by CH_3OH uptakes. **b** CH_3OH uptakes on bulk TiO_2 and V_2O_5, as well as 2% and 10% V_2O_5/TiO_2, as a function of time-on-stream [0.1 kPa CH_3OH, balance He, 0.005–0.1 m^3 $(g_{cat}\ h)^{-1}$, 423 K]. **c** Correlation between the exposed TiO_2 site density ($atom_{Ti}\ nm^{-2}$), calculated from **b**, and the site time yield of methyl formate [10^{-8} mol $(m^2_{cat}\ s)^{-1}$] for a series of V_2O_5/TiO_2 catalysts [1.0 kPa CH_2O, balance He, 0.014–0.05 m^3 $(g_{cat}\ h)^{-1}$, 423 K]. Modified from Ref. [21]

2.3 Case Study III: Distinguishing the Kinetic Significance of Multiple Reaction Pathways and Active Sites in $HCOOCH_3$ Synthesis

During methanol partial oxidation on oxides (in Scheme 2), $HCOOCH_3$ formation could occur via three secondary, concomitant paths (Pathways 4a and 4c, 5, 6a and 6b), and their kinetic prevalence varies with the relative abundances of the various types of active sites, as depicted in Fig. 4a and described here using the case of supported vanadium oxide (VO_x) domains (1–10 wt.%) dispersed on TiO_2 as the example. On VO_x/TiO_2 catalysts, there are (i) redox metal–oxygen site pairs of VO_x (V^{5+}-O^{2-}), where the O^{2-} catalyzes Pathway 4c or 6a, and (ii) Lewis acid–base site pairs of VO_x ($V^{\delta+}$-O^{2-}) that catalyze Pathway 5, as well as (iii) Lewis acid–base pairs of exposed TiO_2 ($Ti^{\delta+}$-O^{2-}), that also catalyze Pathway 5. The relative abundance of these sites depends on the VO_x loading and the corresponding domain size, as well as the surface area of the TiO_2 support.

The specific methyl formate formation rate, r''_{MF} (superscript $''$ denotes normalization per surface area), contains contributions from four separate rate terms ($r_{i,j}[T]_j$, where i denotes Pathway 4, 5, or 6 and j denotes the active site of V or Ti):

$$r''_{MF}\left[\frac{mol}{m^2_{cat}s}\right] = \sum_{j=V,Ti}\sum_{i=4,5,6}\left(r_{i,j}\left[\frac{mol}{mol_{sites}s}\right] \times [T]_j\left[\frac{mol_{sites}}{m^2_{cat}}\right]\right) \tag{23}$$

$r_{i,j}[T]_j$ represents the individual turnover rate of pathway i (per site j) multiplied by its respective site density, $[T]_j$. Each individual turnover rate expression, following Types I–III in Eqns. 5, 6, 7 is expanded as:

$$r_{4,V}(Type-III) = \frac{k_{eff,4c,V}\left[CH_2O\right]\left[CH_3OH\right]\left[V^{5+}-O^{2-}\right]_R}{\left[T_{V^{5+}-O^{2-}}\right]_R} \tag{24}$$

$$r_{5,V}(Type-II) = \frac{k_{eff,5,V}\left[CH_2O\right]^2\left[V^{\delta+}-O^{2-}\right]^2_L}{\left[T_{V^{\delta+}-O^{2-}}\right]^2_L} \tag{25}$$

$$r_{5,Ti}(Type-II) = \frac{k_{eff,5,Ti}\left[CH_2O\right]^2\left[Ti^{\delta+}-O^{2-}\right]^2_L}{\left[T_{Ti^{\delta+}-O^{2-}}\right]^2_L} \tag{26}$$

$$r_{6,V}(Type-I) = \frac{k_{eff,6a,V}\left[CH_2O\right]\left[V^{5+}-O^{2-}\right]_R}{\left[T_{V^{5+}-O^{2-}}\right]_R} \tag{27}$$

where subscript R denotes redox sites, and L denotes Lewis acid–base sites. To evaluate the relative contributions of each rate term (Eqns. 24, 25, 26, 27) to the specific methyl formate formation rate, we would first need to quantify the surface densities of the various active sites, i.e., the $\left[T_{V^{5+}-O^{2-}}\right]_R$, $\left[T_{V^{\delta+}-O^{2-}}\right]_L$, and $\left[T_{Ti^{\delta+}-O^{2-}}\right]_L$ (per exposed surface area) terms in Eqns. 24, 25, 26, 27 including those on the TiO_2 support. Then, we would decouple the rate contributions of each pathway by incorporating CH_2O intermediates into CH_3OH-O_2 reaction feeds and carrying out isotopic labeling/exchange studies.

From the series of 0–10 wt.% V_2O_5/TiO_2 catalysts, where the V_2O_5 contents correspond to up to two monolayer equivalents dispersed on TiO_2,[21] the surface densities of the total [V^{5+}-O^{2-}] site pairs (in $atom_{V\text{-}O}\ nm^{-2}$) were determined from dividing the molar loading ($mol_{V_2O_5}g^{-1}_{cat}$) by the BET surface area ($m^2_{cat}\ g_{cat}^{-1}$). For each catalyst, the surface densities of exposed [Ti^{4+}-O^{2-}] site pairs (in $atom_{Ti\text{-}O}\ nm^{-2}$) were quantified with CH_3OH chemical titration, in an uptake study, since CH_3OH would selectively adsorb on TiO_2 due to its substantially larger adsorption equilibrium constant, i.e., > 1000 kPa^{-1} on TiO_2 versus 4 kPa^{-1} on V_2O_5 at 423 K [21]. Given these equilibrium

constants, the occupation of CH_3OH on [Ti^{4+}-O^{2-}] sites would essentially reach saturation (θ_{CH_3OH}>0.99) whereas that on [V^{5+}-O^{2-}] sites remain less than 0.3, evaluated at 0.1 kPa methanol and 423 K.

Shown in Fig. 4b are the CH_3OH uptakes on 2% and 10% V_2O_5/TiO_2 catalysts, together with those on the bulk TiO_2 and V_2O_5 references. On the bare TiO_2 surfaces, CH_3OH uptakes normalized by the BET surface area reach saturation at 6.5 CH_3OH nm^{-2}. Using the theoretical surface density of [Ti^{4+}-O^{2-}] sites from the terminal (101) facet of anatase of 5.5 $atom_{Ti}$ nm^{-2},[61, 62] this CH_3OH saturation point corresponds to a CH_3OH-to-Ti ratio of 1.1. For the 2% and 10% V_2O_5/TiO_2 catalysts, the final uptakes of CH_3OH are lower than that on TiO_2, as expected because the dispersed V_2O_5 (blue) covers a portion of the TiO_2 support (gray), captured schematically in Fig. 4a. Assuming that methanol adsorbs on the exposed TiO_2 at the same CH_3OH-to-Ti ratio (1.1) as the bare TiO_2, the ratio of CH_3OH uptakes on the supported V_2O_5 catalysts $\left[CH_3OH\right]_{ads,catalyst}$ (units of CH_3OH nm^{-2}) relative to that on the bare TiO_2 surface $\left[CH_3OH\right]_{ads,bareTiO_2}$, together with the surface density of [Ti^{4+}-O^{2-}] sites on TiO_2 of 5.5 $atom_{Ti}$ nm^{-2}, would give the exposed Ti site density:

$$\left[Ti^{4+}-O^{2-}\right]_{catalyst}=\left[Ti^{4+}-O^{2-}\right]_{bareTiO_2}\times\left(\frac{\left[CH_3OH\right]_{ads,catalyst}-\left[CH_3OH\right]_{ads,bulkV_2O_5}}{\left[CH_3OH\right]_{ads,bareTiO_2}}\right) \quad (28)$$

To remove the contributions of CH_3OH adsorption on the VO_x domains, the final uptake on the catalyst $\left[CH_3OH\right]_{ads,catalyst}$ is corrected by subtracting the uptakes on bulk V_2O_5, $\left[CH_3OH\right]_{ads,bulkV_2O_5}$. With the known [$Ti^{4+}$-$O^{2-}$] surface density, the remaining portion of the surface corresponds to the VO_x surface density (blue in Fig. 4a), where the [V^{5+}-O^{2-}] site density depends on whether the VO_x loading is below or above the monolayer value, 7 $atom_{V\text{-}O}$ nm^{-2} [63, 64]. For loadings below one monolayer, the [V^{5+}-O^{2-}] site density equals the total VO_x loading (in $atom_{V\text{-}O}$ nm^{-2}), assuming the vanadium is evenly dispersed on the surface and does not form any crystalline domains, and above the monolayer, equals 7 $atom_{V\text{-}O}$ nm^{-2}, because additional vanadium loaded above the monolayer would deposit on top of exposed vanadium.

This CH_3OH titration technique gives the relative abundance of [Ti^{4+}-O^{2-}] and [V^{5+}-O^{2-}] on the surface of V_2O_5/TiO_2 catalysts, and therefore the quantitative values of the site densities, $[T]_j$ in Eq. 23. As vanadium loading increases, the [Ti^{4+}-O^{2-}] site density decreases, because TiO_2 domains are increasingly covered by VO_x ones–the *x*-axis of Fig. 4c shows this decrease of [Ti^{4+}-O^{2-}] with increasing vanadium loading.

After obtaining the site densities, the next step is to determine which of the rates in Eqns. 24, 25, 26, 27 contribute most significantly to the observed $HCOOCH_3$ formation rate in CH_3OH-O_2 catalysis. First, we remove the kinetic bottleneck of CH_2O formation in the methanol ODH reaction (Pathway 2) by cofeeding CH_2O intermediates. In order to decouple Pathways 4–6 that produce $HCOOCH_3$, we examine the identity of the reactant molecules that participate in these pathways and consider the effects of their removal from the reaction mixtures. In particular, Pathway 5 can occur in the absence of CH_3OH and O_2 reactants, so r_{MF} measured with CH_2O as the sole reactant would allow us to determine the rate contribution of Pathway 5 to the overall rate.

Table 1 shows that, on both TiO_2 and 2% V_2O_5/TiO_2 catalysts, the methyl formate rates in CH_2O feed (without CH_3OH and O_2), r''_{MF,CH_2O}, are in fact higher than those in CH_3OH-O_2-CH_2O feeds, $r''_{MF,CH_3OH-O_2-CH_2O}$, when comparing them at the same CH_2O partial pressure at 423 K. This indicates that Pathway 5 dominates on these catalyst surfaces and Pathways 4 and 6 are negligible. Thus, the rate expression in Eq. 23 can be simplified to contain only the contributions from the Lewis acid–base sites:

$$r''_{MF}=\left(r_{5,V}\times\left[T_{V^{\delta+}-O^{2-}}\right]_L\right)+\left(r_{5,Ti}\times\left[T_{Ti^{\delta+}-O^{2-}}\right]_L\right) \quad (29)$$

Previous studies have shown that both V_2O_5 and TiO_2 could catalyze the Tishchenko reaction in similar operating conditions [50]; in order for us to deconvolute the relative contributions of $Ti^{\delta+}$-O^{2-} and $V^{\delta+}$-O^{2-} site pairs on the rates, we compare the $HCOOCH_3$ formation rates in CH_2O feeds (without CH_3OH nor O_2) for V_2O_5/TiO_2 catalysts with varying $Ti^{\delta+}$-O^{2-} site densities given in Fig. 4b. As the $Ti^{\delta+}$-O^{2-} site density increases with decreasing vanadium loading, the $HCOOCH_3$ formation rates proportionally increase, as captured in Fig. 4c. This linear has unambiguously confirmed that methyl formate is formed exclusively on the $Ti^{\delta+}$-O^{2-} sites. For this reason, the rate equation (Eq. 29) could be simplified further, by removing of the rate term associated with the $V^{\delta+}$-O^{2-} sites:

Table 1 Methyl formate formation rates with various reactant feed compositions and C–H/C–D kinetic isotope effects at 423 K

Catalyst/Feed:	r''_{MF}[10^{-8} mol (m^2_{cat} s)$^{-1}$] [a]			r_{C-H}/r_{C-D} KIE
	CH_3OH-O_2-CH_2O	CH_2O	CD_2O	
TiO_2	1.0	4.4	3.6	1.2
2% V_2O_5/TiO_2	0.3	1.5	1.3	1.2

[a] 0 or 1 kPa CH_3OH, 0 or 20 kPa O_2, 1 kPa CH_2O, balance He. TiO_2: 0.015 m^3 (g_{cat} h)$^{-1}$, 2% V_2O_5/TiO_2: 0.03 m^3 (g_{cat} h)$^{-1}$. From Ref. [21]

$$r''_{MF} = \frac{k_{eff,5,Ti} P^2_{CH_2O} \left[Ti^{\delta+} - O^{2-}\right]^2_L}{\left[T_{Ti^{\delta+}-O^{2-}}\right]^2_L} \left[T_{Ti^{\delta+}-O^{2-}}\right]_L \quad (30)$$

These techniques, when combined together, provide conclusive evidence that Tishchenko reaction (Pathway 5), occurring on the $Ti^{\delta+}$-O^{2-} sites, is the predominant path for methyl formate formation.

Lastly, even within the Tishchenko catalytic cycle, there are multiple plausible sequences of elementary steps leading to $HCOOCH_3$ formation. There are two cases where: (i) CH_2O could undergo kinetically-relevant dehydrogenation to form a surface formate species, before the C–O bond formation with a second CH_2O molecule or (ii) two CH_2O molecules could undergo kinetically-relevant C–O bond formation to form a CH_2OCH_2O species, followed by a 1,3-hydride shift. The exact catalytic sequence could be probed with isotopic labeling/exchange studies. If Case (i) prevails, one would expect a primary C–H/C–D kinetic isotope effect (KIE) that is greater than 2.0, based on the KIEs of other reactions where C–H scission is kinetically relevant [58, 65, 66], whereas if Case (ii) prevails, one would expect a much weaker, secondary C–H/C–D KIE, much closer to unity. As shown in Table 1, the KIE values are approximately 1.2 for both the TiO_2 and 2% V_2O_5/TiO_2 catalysts at 423 K, which is consistent with Case (ii) as the proper sequence of elementary steps.

The approaches highlighted in this case study could be applied to investigate other catalytic systems with multiple pathways, catalyzed by different types of active sites, that form the same product. For example, cofeeding intermediates to decouple the rate contributions from various pathways has been successful in deciphering: (i) methanol to hydrocarbons on zeolite catalysts, where Koch carbonylation leading to C–C bond formation and methyl acetate intermediates was found to dominate, based on CO cofeeding experiments and solid-state NMR spectroscopy [67], and (ii) O_2 reduction on M–N–C catalysts, where hydroquinone-mediated pathways were found to dominate over electrochemical ones based on quinone reaction orders, adsorption isotherms, and H^+/D^+ isotope exchanges [68]. Other relevant catalytic systems where these approaches could be used include: (i) ethanol to butadiene, where butadiene could form through either alcohol- or carbanion-mediated pathways, occurring on bifunctional metal oxides with redox and acid–base functions [69], (ii) butanal to C_6–C_{16} aromatics, where aldehydes are dehydrogenated through either aldol condensation or transfer hydrogenation reactions, occurring on Brønsted acid sites [70]; and (iii) various cascading reactions in cellulose valorization, including glucose to levulinic acid, which could proceed through hydroxymethylfurfural intermediates or direct dehydration of glucose, occurring on Lewis or Brønsted acid sites [71].

3 Comparing Intrinsic Reactivities of Different Reactions on Sulfided Ru Catalysts

Measured rates on surface (Eqns. 1–7) contains a numerator term and a denominator term—the former reflects, from transition state theory, the activation free energies for the reactant (in the gas phase) to evolve the kinetically relevant transition state and the latter the sum of the various adsorbates and the vacant site ($[T_{M\text{-}L}]$, Eq. 4). Both energies in the numerator and denominator terms can be evaluated with computational methods and modeled with kinetic Monte Carlo methods. Here, we describe two strategies on obtaining the reactivity trends across different reactants, by accounting for their difference in the heat of adsorption and the potential coverage effects that appear in the denominator of the rate expression that could contribute to the measured, effective activation barriers, thus allowing us to extract the difference in kinetic properties among the reactants that show up in the numerator of the rate expression.

3.1 Case Study IV: Independent Reactions with Simultaneous Rate Data Fitting–Hydrogenation of Pyridine and Pyrrole on Sulfided Ru Surfaces

Scheme 1b shows the reactive hydrogen species generated from the activation of H_2 and H_2S and their attacks on N-heterocycles on sulfide surfaces as a part of the catalytic events in hydrotreatment catalysis. The hydrogenation of the N-heterocycles does not consume or produce sulfur, therefore the sulfur chemical potential of ruthenium is set by the H_2S-to-H_2 fugacity ratio $[(f_{H_2S})^{\alpha}(f_{H_2})^{\beta}$, $0 \le \alpha \le 1$, $-1 \le \beta \le 1]$ through the chemical equilibrium of the RuS_2-H_2S-H_2 system [8]:

$$Ru + xH_2S \leftrightharpoons RuS_x + xH_2 \quad (31)$$

$$\frac{a_{RuS_x}}{a_{Ru}} = K_{RuS_x} \frac{f_{H_2S}}{f_{H_2}} \quad (32)$$

where a_i denotes the activity of species i. This ratio also dictates the surface abundances of the Ru^{n+}-S^{2-}, Ru^{n+}-$(H^{\delta-})$-S^{2-}-$(H^{\delta+})$, and Ru^{n+}-(SH_2)-S^{2-} site pairs, as found on S-deficient sulfided Ru surfaces (Scheme 1b):

$$H_2 + Ru^{n+} - S^{2-} \rightleftharpoons Ru^{n+} - (H^{\delta-}) - S^{2-} - (H^{\delta+}) \quad (33)$$

$$\frac{a_{Ru^{n+}-(H^{\delta-})-S^{2-}-(H^{\delta+})}}{a_{Ru^{n+}-S^{2-}}} = K_{H_2,RuS_x} f_{H_2} \quad (34)$$

$$H_2S + Ru^{n+} - S^{2-} \leftrightharpoons Ru^{n+} - (SH_2) - S^{2-} \quad (35)$$

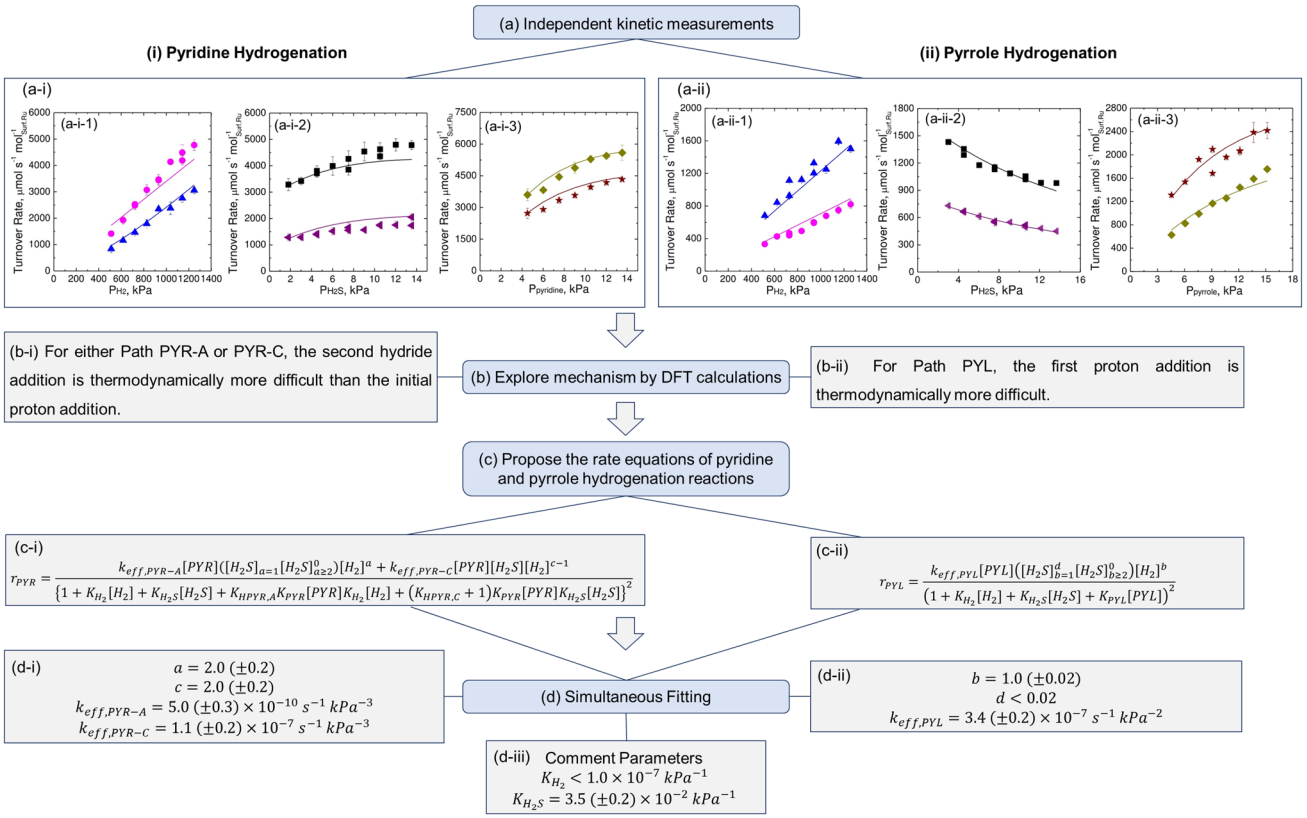

Scheme 3 Flow chart of **a** kinetic measurements by varying partial pressures of (a-i-1, and a-ii-1) H_2, (a-i-2, and a-ii-2) H_2S, and (a-i-3, and a-ii-3) pyridine or pyrrole, **b** DFT calculations, **c** rate equation derivation, and **d** the simultaneous fittings of (a–i, b–i, c–i, d–i) pyridine and (a–ii, b–ii, c–ii, d–ii) pyrrole hydrogenation at 573 K, 1.5 MPa [1.8 kPa H_2S (★, ▲), 13.5 kPa H_2S (◆, ●), 616 kPa H_2 (◄), 1250 kPa H_2 (★, ◆, ■), and 6.0 kPa pyridine/pyrrole (■, ◄, ▲, ●)], and 4.5×10^{-2} $m^3\ h^{-1}\ g^{-1}$ gas hourly space velocity. Lines in (a–i) and (a–ii) the kinetic fittings predicted from Eqns. c–i and c–ii, respectively. Eqns. c–i and c–ii are Eqns. 41 and 42, with definitions of parameters given in Sect. 3.1. Data are reproduced from Ref. [8]

$$\frac{a_{Ru^{n+}-(SH_2)-S^{2-}}}{a_{Ru^{n+}-S^{2-}}} = K_{H_2S,RuS_x} f_{H_2S} \tag{36}$$

Since there were no net consumption of H_2S, together with a large excess of H_2 in the typical hydrotreatment reactions, Eqns. 33 and 35 must be quasi-equilibrated. Therefore, at a constant temperature, the surface abundances of Ru^{n+}-$(H^{\delta-})$-S^{2-}-$(H^{\delta+})$ and Ru^{n+}-(SH_2)-S^{2-} only depend on $(f_{H_2S})^{\alpha}(f_{H_2})^{\beta}$, regardless of the reaction that they participate in:

$$Ru^{n+} - (SH_2) - S^{2-} + H_2 \rightleftharpoons Ru^{n+} - (H^{\delta-}) - S^{2-} - (H^{\delta+}) + H_2S \tag{37}$$

$$\frac{a_{Ru^{n+}-(H^{\delta-})-S^{2-}-(H^{\delta+})}}{a_{Ru^{n+}-(SH_2)-S^{2-}}} = K_{H_2S-H_2,RuS_x} \frac{f_{H_2}}{f_{H_2S}} \tag{38}$$

Bader charge analysis carried out on the various reactive hydrogen species, provided in Scheme 1b, has shown that the S^{2-}-$(H^{\delta+})$ and Ru^{n+}-(SH_2) species exhibit slightly positive charge and Ru^{4+}-$(H^{\delta-})$ slightly negative charge (Scheme 1b-i). These different types of reactive hydrogen acquire different catalytic roles in the sequential hydrogen attack reactions on the N-heteroarenes.

Schemes 3a–i and a-ii show the measured turnover rates of pyridine and pyrrole hydrogenation, respectively [573 K, 1.5 MPa (1.8–13.5 kPa H_2S, 510–1250 kPa H_2, 4.5–15.0 kPa pyridine/pyrrole) and 4.5×10^{-2} $m^3\ h^{-1}\ g^{-1}$ gas hourly space velocity]. The non-linear regression of these turnover rates in Scheme 3a–i (or Scheme 3a–ii) with Eq. 39 (or Eq. 40) gives the effective reaction orders of H_2, H_2S, and pyridine/pyrrole (denoted as α_j, β_j, and γ_j, respectively; subscript $j = PYR$ or PYL, which represents pyridine or pyrrole, respectively).

$$r_{PYR} = k_{PYR-eff}\left[H_2\right]^{\alpha_{PYR}}\left[H_2S\right]^{\beta_{PYR}}[PYR]^{\gamma_{PYR}} \tag{39}$$

$$r_{PYL} = k_{PYL-eff}\left[H_2\right]^{\alpha_{PYL}}\left[H_2S\right]^{\beta_{PYL}}[PYR]^{\gamma_{PYL}} \tag{40}$$

where k_{j-eff} is the effective rate constant. Comparing the cases of pyridine, a more basic molecule, versus pyrrole, a less basic molecule, the effective reaction orders towards H_2 are 1.30 (±0.04) versus 1.08 (±0.05), towards the

N-heterocycles are 0.31 (±0.06) vs. 0.60 (±0.05), and towards the H_2S are 0.19 (±0.02) versus − 0.26 (±0.01), respectively (Scheme 3). These differences in effective reaction orders arise from the difference in the hydrogen attack sequences, the reactive hydrogen species that participate in the H attack reaction, the electronic properties of N-heterocycles, and the kinetic relevance of hydrogen addition events. According to Eqns. 5–7, the later H addition as the kinetically relevant step will increase the reaction order of H_2 in the numerator, and the coverages of hydrogen species, sulfur species and N-intermediates in the denominator of the rate equation will also impact the effective reaction orders.

Pyridine is a basic molecule, due to the localization of lone pair electrons from its N atom. Therefore, pyridine hydrogenation initiates with the addition of either S^{2-}-$H^{\delta+}$ (Path PYR-A) or Ru^{n+}-(SH_2) proton (Path PYR-C), followed by the attack of Ru^{n+}-$H^{\delta-}$ hydride, in which the latter is thermodynamically more difficult than the former (Scheme 1b–i). Pyrrole is a non-basic molecule, since its nitrogen lone pair electrons are delocalized in the aromatic ring. For this reason, pyrrole, unlike pyridine, would accept the proton from S^{2-}-$H^{\delta+}$ species in a thermodynamically and therefore kinetically more difficult reaction, followed by accepting a hydride from Ru^{n+}-$H^{\delta-}$ species (Path PYL, Scheme 1b–i), as established with DFT calculations. The rate expressions of pyridine and pyrrole hydrogenation at 573 K are (also given in Scheme 3c-i and c-ii, respectively) [8]:

$$r_{PYR} = \frac{k_{eff,PYR-A}[PYR]\left(\left[H_2S\right]_{a=1}\left[H_2S\right]_{a\geq 2}^{0}\right)\left[H_2\right]^{a} + k_{eff,PYR-C}[PYR]\left[H_2S\right]\left[H_2\right]^{c-1}}{\left\{1 + K_{H_2}\left[H_2\right] + K_{H_2S}\left[H_2S\right] + K_{HPYR,A}K_{PYR}[PYR]K_{H_2}\left[H_2\right] + \left(K_{HPYR,C}+1\right)K_{PYR}[PYR]K_{H_2S}\left[H_2S\right]\right\}^{2}} \tag{41}$$

$$r_{PYL} = \frac{k_{eff,PYL}[PYL]\left(\left[H_2S\right]_{b=1}^{d}\left[H_2S\right]_{b\geq 2}^{0}\right)\left[H_2\right]^{b}}{\left(1 + K_{H_2}\left[H_2\right] + K_{H_2S}\left[H_2S\right] + K_{PYL}[PYL]\right)^{2}} \tag{42}$$

r_j and $k_{eff,j}$ are the turnover rate and effective rate coefficient of pyridine or pyrrole hydrogenation, respectively (subscripts *PYR* and *PYL* denote pyridine and pyrrole hydrogenation, respectively, and subscripts *PYR-A* and *PYL-C* denote Paths PYR-A and PYR-C, respectively). Superscripts a and c ($1 \leq a \leq 6$, $1 \leq c \leq 6$) represent the number of a^{th} and c^{th} H additions as the kinetically relevant steps in Paths PYR-A and PYR-C, respectively. Superscript b ($1 \leq b \leq 4$) represents the number of b^{th} H addition that limits turnover rates in Path PYL. Superscript d equals 0 or 1, indicating the adsorption of pyrrole on Ru^{4+}-S^{2-} or Ru^{4+}-(SH_2)-S^{2-}, respectively. K_ζ is the equilibrium constant of Step ζ in Scheme 1b–i. Since equilibrium constants are only functions of temperature, the values of K_{H2} and K_{H2S} would remain the same in both pyridine and pyrrole hydrogenation catalysis. Thus, one can carry out regression of the rate data for both reactions by simultaneously regressing Eqns. 41 and 42 against the rate data from the respective reactions, by setting K_{H2} and K_{H2S} values the same across both pyridine and pyrrole hydrogenation reactions. As shown in Scheme 3, the equilibrium constants of H_2 dissociation and H_2S adsorption are determined to be 1.0×10^{-7} kPa^{-1} and 3.5 (±0.2)$\times10^{-2}$ kPa^{-1}, respectively. Both values of a and c are 2.0 (±0.2), indicating that the second H addition steps in both Paths PYR-A and PYR-C limit rates, and b and d are 1.0 (±0.02) and < 0.02, respectively, suggesting that pyrrole prefers to adsorb on the Ru^{4+}-S^{2-} site pair and the initial proton addition in Path PYL limits the rates. These results of simultaneous fitting agree with DFT calculations. Using similar approaches, another study from our group showed that the 2nd H addition step of cyclohexene hydrogenation and the 3rd or 4th H addition step of pyridine hydrogenation are their respective kinetically relevant steps on both S-covered Pt and Pd surfaces at 573 K [9].

This approach is especially useful for complex rate equations with multiple parameters, since it can constrain the degree of freedom in the rate data fitting to obtain the unique solution of the parameters. In addition, it can assist us with comparing intrinsic reactivities of different reactions carried out independently on the same catalyst and at identical temperature. For example, the general rate expressions of two hydrogenation reactions of Type-II (Eq. 6), denoted as B1-H_2 and B2-H_2, are:

$$r_{bi,\sigma_{B1}=2,B1} = \frac{k_{eff,bi,\sigma_{B1}=2,B1}\left[I_{B1}\right]^{q_{B1}}\left[H_2\right]^{q_{H_2}}\left[M^{n+}-L^{m-}\right]^{\sigma_{B1}}}{\left[T_{M-L}\right]^{\sigma_{B1}}} = \frac{k_{bi,\sigma_{B1}=2,B1}K_{lumpB1}^{q_{B1}}K_{H_2}^{q_{H_2}}\left[I_{B1}\right]^{q_{B1}}\left[H_2\right]^{q_{H_2}}}{\left(\theta+\varphi_{B1}\right)^{\sigma_{B1}}} \tag{43}$$

$$r_{bi,\sigma_{B2}=2,B2} = \frac{k_{eff,bi,\sigma_{B2}=2,B2}\left[I_{B2}\right]^{q_{B2}}\left[H_2\right]^{q_{H_2}}\left[M^{n+}-L^{m-}\right]^{\sigma_{B2}}}{\left[T_{M-L}\right]^{\sigma_{B2}}} = \frac{k_{bi,\sigma_{B2}=2,B2}K_{lumpB2}^{q_{B2}}K_{H_2}^{q_{H_2}}\left[I_{B2}\right]^{q_{B2}}\left[H_2\right]^{q_{H_2}}}{\left(\theta+\varphi_{B2}\right)^{\sigma_{B2}}} \tag{44}$$

where each parameter of σ_{B1} and σ_{B2} equals either one or two, depending on the number of active sites needed for the kinetically relevant step, and $k_{bi,\sigma_{B1}=2,B1}$ (or $k_{eff,bi,\sigma=2,B1}$) and $k_{bi,\sigma_{B2}=2,B2}$ (or $k_{eff,bi,\sigma=2,B2}$) are elementary rate constants (or effective rate coefficients) of the kinetically relevant steps of

B1-H_2 and B2-H_2, respectively. $K_{lumpB1}^{q_{B1}}$ and $K_{lumpB2}^{q_{B2}}$ are the lumped equilibrium constants for the formation of the precursors, $[M^{n+}-(I_{b1})-L^{m-}]$ and $[M^{n+}-(I_{b2})-L^{m-}]$, of the kinetically relevant steps. Superscript q_{H_2} equals 0.5 or 1.0, depending on the hydrogen species involved in the kinetically relevant step. φ_{B1} and φ_{B2} relate to the coverage of B1- and B2-derived species, respectively, and θ relates to the sum of coverages of hydrogen species and active site pairs:

$$\varphi_{B1} = K_{lumpB1}\left[I_{B1}\right] + \varphi_{otherB1} \tag{45}$$

$$\varphi_{B2} = K_{lumpB2}\left[I_{B2}\right] + \varphi_{otherB2} \tag{46}$$

$$\theta = 1 + \left(K_{H_2}\left[H_2\right]\right)^{q_{H_2}} + \theta_{otherH} \cdots \tag{47}$$

$\varphi_{otherB1}$ and $\varphi_{otherB2}$ denotes the coverage ratio of other B1 and B2 derived species to the active site pairs, respectively. θ_{otherH} denotes the coverage ratio of other hydrogen species to the active site pairs. Since the equilibrium constant values describing the hydrogen dissociative adsorption are identical for both reactions, we could obtain the values of elementary rate constants, $k_{bi,\sigma_{B1}=2,B1}$ and $k_{bi,\sigma=2,B2}$, where their ratio reflects the relative reactivities of the kinetically relevant steps of B1-H_2 and B2-H_2, through simultaneous rate data regressions of Eqns. 43 and 44. For example, when we compare Path PYR-A of pyridine hydrogenation and Path PYL of pyrrole hydrogenation, although the former exhibited a much lower effective rate coefficient [5.0 ($\pm$0.3)$\times10^{-10}$ s^{-1} kPa^{-3} (Scheme 3d–i) vs. 3.4 ($\pm$0.2)$\times10^{-7}$ s^{-1} kPa^{-2} (Scheme 3d-ii)], the ratio of the elementary rate constants of kinetically relevant step of Path PYR-A to that of Path PYL is 1.4, calculated from the parameters reported in Ref [8], indicating that this path indeed has a higher elementary rate constant. This reveals that the lower effective rate coefficient of Path PYR-A is hindered by the lower equilibrium constant of the formation of the protonated pyridine precursor of the kinetically relevant step.

3.2 Case Study V: Competitive Reactions: Effective Rate Coefficient Ratio–Hydrogenation of Carbonyls on Sulfided Ru Surfaces

In contrast to Case Study IV above, which compares the intrinsic catalytic reactivities by independently carrying out the reactions on catalysts at the same temperature, another approach, described here, is to simultaneously carry out the reactions with two or more reactants. The measured rate ratio would simply reflect the ratio of the numerator terms in the rate equation, providing that the reactions occur on the same active sites. For example, the turnover rate ratio of two Type-I reactions (denoted as A1 and A2) is:

$$\frac{r_{uni,\sigma=1,A1}}{r_{uni,\sigma=1,A2}} = \frac{\frac{k_{eff,uni,\sigma=1,A1}\left[I_{A1}\right]^{q_{A1}}\left[M^{n+}-L^{m-}\right]}{\left[T_{M-L}\right]}}{\frac{k_{eff,uni,\sigma=1,A2}\left[I_{A2}\right]^{q_{A2}}\left[M^{n+}-L^{m-}\right]}{\left[T_{M-L}\right]}} = \frac{k_{eff,uni,\sigma=1,A1}\left[I_{A1}\right]^{q_{A1}}}{k_{eff,uni,\sigma=1,A2}\left[I_{A2}\right]^{q_{A2}}} \tag{48}$$

where subscripts A1 and A2 represent the reactions of A1 and A2. Since the reactions occur on the same sites, the denominators of the rate equations, which reflect the coverages of various surface species, are equal and can be canceled out. If the reaction orders of I_{A1} and I_{A2} are same during their respective kinetically relevant step ($q_{A1} = q_{A2}$) and I_{A1} and I_{A2} partial pressures are identical during the reactions ($\left[I_{A1}\right] = [I_{A2}]$), the turnover rate ratio will equal to the effective rate coefficient ratio,

$$\frac{r_{uni,\sigma=1,A1}}{r_{uni,\sigma=1,A2}} = \frac{k_{eff,uni,\sigma=1,A1}}{k_{eff,uni,\sigma=1,A2}} \tag{49}$$

This strategy is also applicable to Type-II and Type-III reactions.

Our previous study[7] explored the hydrogenation reactivities of aliphatic ketones and aldehydes ($R^aC(O)R^b$; $R^a = CH_3/C_2H_5/C_3H_7$, and $R^b = CH_3$ for ketones; $R^a = C_2H_5/C_3H_7/C_4H_9$ and $R^b = H$ for aldehydes) on S-deficient sulfided Ru catalysts at 503 K by using the competitive reaction strategy. As shown in Fig. 5a, the turnover rate ratio ($r_{R^aC(O)R^b}(r_{R^1C(O)R^b_{ref}})^{-1}$) of $R^aC(O)R^b$ to a reference reactant ($R^1C(O)R^b_{ref}$; $R^1 = CH_3$ or C_2H_5 for ketone or aldehyde, respectively) increases with the increasing hydride affinity of $R^aC(O)R^b$ ($HA_{R^aC(O)R^b}$). The combination of isotopic studies and DFT calculations have established that the carbonyl hydrogenation initiates with the kinetically relevant addition of the Ru^{n+}-$H^{\delta-}$ hydride at the carbonyl C atom followed by the second addition of the S^{2-}-$H^{\delta+}$ proton at the O atom. Therefore, the rate expression for carbonyl hydrogenation is:

$$r_{R^aC(O)R^b} = \frac{k_{R^aC(O)R^b}K_{R^aC(O)R^b}K_{H_2}\left[R^aC(O)R^b\right]\left[H_2\right]}{\left[T_{M-L}\right]} \tag{50}$$

where the denominator $[T_{M\text{-}L}]$ represents the total coverage of surface species, $k_{R^aCH(O)R^b}$ is the rate constant of the kinetically relevant step, and $K_{R^aC(O)R^b}$ and K_{H_2} are the equilibrium constants of $R^aC(O)R^b$ adsorption and H_2 dissociation, respectively.

If the partial pressures of $R^aC(O)R^b$ and the reference reactant ($R^1C(O)R^b_{ref}$) are identical during the reactions, the terms $[R^aC(O)R^b]$ and $[H_2]$ in the numerator and the term $[T_{M\text{-}L}]$ in the denominator can be cancelled out when comparing their rates.

$$\frac{r_{R^aC(O)R^b}}{r_{R^1C(O)R^b_{ref}}} = \frac{k_{R^aC(O)R^b,alk}K_{R^aC(O)R^b}}{k_{R^1C(O)R^b_{ref},alk}K_{R^1C(O)R^b_{ref}}} \tag{51}$$

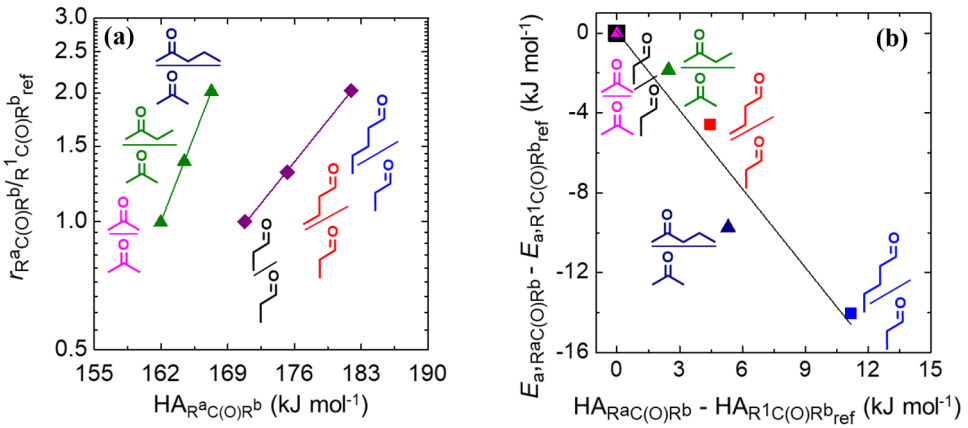

Fig. 5 The correlations of **a** turnover rate ratios of $R^aC(O)R^b$ to $R^1C(O)R^b_{ref}$ ($r_{R^aC(O)R^b}(r_{R^1C(O)R^b_{ref}})^{-1}$) and hydride affinity of $R^aC(O)R^b$ ($HA_{R^aC(O)R^b}$), **b** activation energy difference ($E_{a,R^aC(O)R^b} - E_{a,R^1C(O)R^b_{ref}}$) and hydride affinity difference of $R^aC(O)R^b$ and $R^1C(O)R^b_{ref}$ ($HA_{R^aC(O)R^b} - HA_{R^1C(O)R^b_{ref}}$) for $R^aC(O)R^b$ and $R^1C(O)R^b_{ref}$ hydrogenation reactions at 503 K, 1.5 MPa [1.8 kPa H_2S, 1200 kPa H_2, 13.5 kPa carbonyl compound mixtures (1:1:1 molar ratio of either propanal/butanal/pentanal mixture or acetone/2-butanone/2-pentanone mixture)], 0.18 $m^3\ h^{-1}\ g^{-1}$ gas hourly space velocity. Reproduced from Ref. [7]

The turnover rate ratio, $r_{R^aC(O)R^b}(r_{R^1C(O)R^b_{ref}})^{-1}$, can be further expanded to an expression relating to the activation entropy difference ($\Delta S^{\neq}_{R^aC(O)R^b} - \Delta S^{\neq}_{R^1C(O)R^b_{ref}}$) and activation enthalpy difference ($\Delta H^{\neq}_{R^aC(O)R^b} - \Delta H^{\neq}_{R^1C(O)R^b_{ref}}$). Due to the correlations between the pre-exponential factor and the activation entropy and between the activation barrier and the activation enthalpy, $r_{R^aC(O)R^b}(r_{R^1C(O)R^b_{ref}})^{-1}$ also relates to the pre-exponential ratio ($A_{R^aC(O)R^b}/A_{R^1C(O)R^b_{ref}}$) and the activation barrier difference ($E_{a,R^aC(O)R^b} - E_{a,R^1C(O)R^b_{ref}}$):

$$\frac{r_{R^aC(O)R^b}}{r_{R^1C(O)R^b_{ref}}} = exp\left[\frac{\Delta S^{\neq}_{R^aC(O)R^b} - \Delta S^{\neq}_{R^1C(O)R^b_{ref}}}{R}\right] exp\left[\frac{-\left(\Delta H^{\neq}_{R^aC(O)R^b} - \Delta H^{\neq}_{R^1C(O)R^b_{ref}}\right)}{RT}\right] = \left(\frac{A_{R^aC(O)R^b}}{A_{R^1C(O)R^b_{ref}}}\right) exp\left[\frac{-\left(E_{a,R^aC(O)R^b} - E_{a,R^1C(O)R^b_{ref}}\right)}{RT}\right] \quad (52)$$

Since the effective rate coefficients have a negative dependence on the activation barriers, the negative dependence of activation energy difference of $R^aC(O)R^b$ and $R^1C(O)R^b_{ref}$ hydrogenation ($E_{a,R^aC(O)R^b} - E_{a,R^1C(O)R^b_{ref}}$) on the hydride affinity difference of $R^aC(O)R^b$ and $R^1C(O)R^b_{ref}$ ($HA_{R^aC(O)R^b} - HA_{R^1C(O)R^b_{ref}}$), as shown in Fig. 5b, agrees with the positive dependence of $r_{R^aC(O)R^b}(r_{R^1C(O)R^b_{ref}})^{-1}$ on $HA_{R^aC(O)R^b}$ (Fig. 5a).

According to the Bell-Evans-Polanyi principle [72, 73], the rate ratio can also reflect the difference in the heats of reaction of the kinetically relevant, initial hydride addition to $R^aC(O)R^b$ and $R^1C(O)R^b_{ref}$ ($\Delta E_{1stH,R^aC(O)R^b} - \Delta E_{1stH,R^1C(O)R^b_{ref}}$),

$$\frac{r_{R^aC(O)R^b}}{r_{R^1C(O)R^b_{ref}}} = \left(\frac{A_{R^aC(O)R^b}}{A_{R^1C(O)R^b_{ref}}}\right) exp\left[\frac{-\varepsilon_{carbonyl}\left(\Delta E_{1stH,R^aC(O)R^b} - \Delta E_{1stH,R^1C(O)R^b_{ref}}\right)}{RT}\right] \quad (53)$$

in which $\varepsilon_{carbonyl}$ is a constant factor between zero and one describing the lateness of the transition state. Since $\Delta E_{1stH,R^aC(O)R^b}$ is a function of the hydride affinity ($HA_{R^aC(O)R^b}$), this equation allows us to build the correlation between the intrinsic reactivity and thermodynamic property of the reactions.

As explained above, the strategy of the competitive experiment can remove the coverage effect, and thus can efficiently compare the intrinsic reactivities of different

compounds (Eqns. 48 and 51), especially for the reactants undergo a similar reaction mechanism, and allow us to interpret the intrinsic causes for the reactivity difference (Eq. 53). Employing this approach, our group has also revealed that the hydrogenation reactivities of aliphatic carbonyl compounds in protic solvent-transition metal (Ru, Pt, Pd) interfaces increase with the increasing proton affinities of reactants [74]. On such catalytic interfaces, the hydrogenation reaction occurs via a proton−electron pathway, where a proton generated from H* ionization rapidly interacts with the O atom, followed by a kinetically difficult H* attack at the carbonyl C atom. The carbonyl compound with a higher proton affinity is more stable after accepting a proton, and thus is more reactive in the following kinetically relevant step.

4 Summary

Oxide and sulfide surfaces are structurally complex–they consist of metal cations and O^{2-} or S^{2-} anions with multiple catalytic functions of (i) redox (M^{n+}-O^{2-}), through the involvement of the lattice oxygen (or the equivalent S), (ii) Brønsted acid (M-OH), through the proton bound to the O, and (iii) Lewis acid ($M^{\delta+}$-O^{2-}), through the metal cationic center. They are particularly suitable for catalyzing reactions requiring multiple types of active sites as well as cascade reactions. Due to their structural complexity, it is often challenging to probe quantitatively, for each type of active site, its site density and reactivities (per site). This article describes several experimental approaches in deciphering the reactivity of the sites in oxidation and in hydrogenation catalysis, as they work together, where the catalytic reactions involve dehydration, C–O bond formation, oxidative dehydrogenation (which requires C–H bond scission), and hydrogen attack chemistry to heterocycles and to carbonyls. The methodology involves combined or correlative approaches of introducing titrant to selective titrate and thus depress the functionality of the site, rate measurements under controlled coverages, and isotopic studies. Emphasized here is a correlative approach, combining events that occur during titration and rate measurements, as well as through controlling the surface coverages by setting the chemical potential on the surfaces, with rate expression derived from elementary steps, and rate data regression.

These approaches, shown in various case studies in the article, led to the following findings of: (i) intrinsic kinetic dependencies, after accounting for corruption due to gradual site losses in rate measurements; (ii) correlation in the oxidative dehydrogenation and intermolecular dehydration rates arising from the changes in the reactivity of redox and acid sites; (iii) identifying the most prevalent pathways and the involvement of the active sites, where multiple pathways and types of active sites are potentially involved; and (iv) the kinetic requirements for the evolvement of the kinetically relevant transition states, by controlling the surface coverages, through setting the chemical potential of sulfur (or oxygen) on the catalyst surfaces and the use of competitive reactions.

These methods, each with a different purpose, provide insights on the catalytic steps, reaction paths, and give information on the various terms, i.e., the number of active sites involved in the kinetically relevant step, the rate coefficients, and the reaction orders, which appear in the rate expression, as well as their meaning.

Acknowledgements This work was supported by Suncor Energy Inc., Imperial Oil, Canada Foundation for Innovation (CFI), and the Natural Sciences and Engineering Research Council of Canada (NSERC) through Collaborative Research and Development Grant CRDPJ543577-19 and CRDPJ476457-14. H. Cai acknowledges the financial support from the National Natural Science Foundation of China (NSFC, Grant No. 22208299). G. Cai and W. T. Broomhead acknowledge financial support from the University of Toronto Graduate Student Endowment Fund. We thank A. Rodriguez (Western University) for preparing the bulk $FeMoO_x$ catalysts and W. Tian (Western University) for preparing the VO_x/TiO_2 catalysts.

Funding NSERC, CRDPJ543577-19, Ya-Huei Cathy Chin, CRDPJ476457-14, Ya-Huei Cathy Chin, National Natural Science Foundation of China, 22208299, Haiting Cai

References

1. Abdelgaid M, Mpourmpakis G (2022) Structure−activity relationships in lewis acid−base heterogeneous catalysis. ACS Catal 12:4268–4289. https://doi.org/10.1021/acscatal.2c00229
2. Védrine JC (2002) The role of redox, acid-base and collective properties and of cristalline state of heterogeneous catalysts in the selective oxidation of hydrocarbons. Top Catal 21:97–106. https://doi.org/10.1023/A:1020560200125
3. Metiu H, Chrétien SC, Hu Z et al (2012) Chemistry of lewis acid−base pairs on oxide surfaces. J Phys Chem C 116:10439–10450. https://doi.org/10.1021/jp301341t
4. Jacobsen CJH, Törnqvist E, Topsøe H (1999) HDS, HDN and HYD activities and temperature-programmed reduction of unsupported transition metal sulfides. Catal Lett 63:179–183. https://doi.org/10.1023/a:1019017004845
5. Moses PG, Hinnemann B, Topsøe H, Nørskov JK (2007) The hydrogenation and direct desulfurization reaction pathway in thiophene hydrodesulfurization over MoS_2 catalysts at realistic conditions: a density functional study. J Catal 248:188–203. https://doi.org/10.1016/j.jcat.2007.02.028
6. Šarić M, Rossmeisl J, Moses PG (2018) Modeling the adsorption of sulfur containing molecules and their hydrodesulfurization intermediates on the co-promoted MoS_2 catalyst by DFT. J Catal 358:131–140. https://doi.org/10.1016/j.jcat.2017.12.001
7. Cai H, Schimmenti R, Gradiski MV et al (2021) Mechanistic similarities and differences for hydrogenation of aromatic heterocycles and aliphatic carbonyls on sulfided Ru nanoparticles. ACS Catal 11:12585–12608. https://doi.org/10.1021/acscatal.1c01925

8. Cai H, Schimmenti R, Nie H et al (2019) Mechanistic role of the proton-hydride pair in heteroarene catalytic hydrogenation. ACS Catal 9:9438–9445. https://doi.org/10.1021/acscatal.9b01997
9. Cai H, Chin YHC (2021) Catalytic effects of chemisorbed sulfur on pyridine and cyclohexene hydrogenation on Pd and Pt clusters. ACS Catal 11:1684–1705. https://doi.org/10.1021/acscatal.0c04213
10. Sun R, Delidovich I, Palkovits R (2019) Dimethoxymethane as a cleaner synthetic fuel: synthetic methods, catalysts, and reaction mechanism. ACS Catal 9:1298–1318. https://doi.org/10.1021/acscatal.8b04441
11. Baranowski CJ, Bahmanpour AM, Kröcher O (2017) Catalytic synthesis of polyoxymethylene dimethyl ethers (OME): a review. Appl Catal B 217:407–420. https://doi.org/10.1016/j.apcatb.2017.06.007
12. Carrero CA, Schloegl R, Wachs IE, Schomaecker R (2014) Critical literature review of the kinetics for the oxidative dehydrogenation of propane over well-defined supported vanadium oxide catalysts. ACS Catal 4:3357–3380. https://doi.org/10.1021/cs5003417
13. Gomez E, Kattel S, Yan B et al (2018) (2018) Combining CO_2 reduction with propane oxidative dehydrogenation over bimetallic catalysts. Nat Commun 9:1–6. https://doi.org/10.1038/s41467-018-03793-w
14. Xing F, Nakaya Y, Yasumura S et al (2022) Ternary platinum–cobalt–indium nanoalloy on ceria as a highly efficient catalyst for the oxidative dehydrogenation of propane using CO_2. Nat Catal 5:55–65. https://doi.org/10.1038/s41929-021-00730-x
15. Liu S, Wang H, Wang S et al (2023) Engineering morphology and Ni substitution of $Ni_xCo_{3-x}O_4$ spinel oxides to promote catalytic combustion of ethane: elucidating the influence of oxygen defects. ACS Catal 13:4683–4699. https://doi.org/10.1021/acscatal.3c00286
16. Yuan Y, Brady C, Lobo RF, Xu B (2021) Understanding the correlation between ga speciation and propane dehydrogenation activity on Ga/H-ZSM-5 catalysts. ACS Catal 11:10647–10659. https://doi.org/10.1021/acscatal.1c01497
17. Zhao D, Tian X, Doronkin DE et al (2021) In situ formation of ZnO_x species for efficient propane dehydrogenation. Nature 599:234–238. https://doi.org/10.1038/s41586-021-03923-3
18. Deshlahra P, Iglesia E (2016) Reactivity and selectivity descriptors for the activation of C–H bonds in hydrocarbons and oxygenates on metal oxides. J Phys Chem C 120:16741–16760. https://doi.org/10.1021/acs.jpcc.6b04604
19. Yan H, He K, Samek IA et al (2021) Tandem In_2O_3-Pt/Al_2O_3 catalyst for coupling of propane dehydrogenation to selective H_2 combustion. Science 371:1257–1260
20. Zabilska A, Clark AH, Moskowitz BM et al (2022) Redox dynamics of active VO_x sites promoted by TiO_x during oxidative dehydrogenation of ethanol detected by operando quick XAS. JACS Au 2:762–776. https://doi.org/10.1021/jacsau.2c00027
21. Broomhead WT, Tian W, Herrera JE, Chin YHC (2022) Kinetic coupling of redox and acid chemistry in methanol partial oxidation on vanadium oxide catalysts. ACS Catal 12:11801–11820. https://doi.org/10.1021/acscatal.2c01852
22. Deshlahra P, Carr RT, Chai SH, Iglesia E (2015) Mechanistic details and reactivity descriptors in oxidation and acid catalysis of methanol. ACS Catal 5:666–682. https://doi.org/10.1021/cs501599y
23. Chen K, Iglesia E, Bell AT (2001) Isotopic tracer studies of reaction pathways for propane oxidative dehydrogenation on molybdenum oxide catalysts. J Phys Chem B 105:646–653. https://doi.org/10.1021/jp002100x
24. Kwon S, Deshlahra P, Iglesia E (2018) Dioxygen activation routes in Mars-van Krevelen redox cycles catalyzed by metal oxides. J Catal 364:228–247. https://doi.org/10.1016/J.JCAT.2018.05.016
25. Christiansen MA, Mpourmpakis G, Vlachos DG (2013) Density functional theory-computed mechanisms of ethylene and diethyl ether formation from ethanol on γ-Al_2O_3(100). ACS Catal 3:1965–1975. https://doi.org/10.1021/cs4002833
26. Otero Areán C, Bellan AL, Mentruit MP et al (2000) Preparation and characterization of mesoporous γ-Ga_2O_3. Microporous Mesoporous Mater 40:35–42. https://doi.org/10.1016/S1387-1811(00)00240-7
27. Scaranto J, Giorgianni S (2008) A quantum-mechanical study of CO adsorbed on TiO_2: a comparison of the Lewis acidity of the rutile (110) and the anatase (101) surfaces. J Mol Struct 858:72–76. https://doi.org/10.1016/j.theochem.2008.02.027
28. Abee MW, Cox DF (2002) NH3 chemisorption on stoichiometric and oxygen-deficient SnO_2(110) surfaces. Surf Sci 520:65–77. https://doi.org/10.1016/S0039-6028(02)02247-1
29. Roy S, Mpourmpakis G, Hong D-Y et al (2012) Mechanistic study of alcohol dehydration on γ-Al_2O_3. ACS Catal 2:1846–1853. https://doi.org/10.1021/cs300176d
30. Jenness GR, Christiansen MA, Caratzoulas S et al (2014) Site-dependent Lewis acidity of γ-Al_2O_3 and its impact on ethanol dehydration and etherification. J Phys Chem C 118:12899–12907. https://doi.org/10.1021/jp5028349
31. Christiansen MA, Mpourmpakis G, Vlachos DG (2013) Density functional theory-computed mechanisms of ethylene and diethyl ether formation from ethanol on γ-Al_2O_3 (100). ACS Catal 3:1965–1975. https://doi.org/10.1021/cs4002833
32. Kostetskyy P, Mpourmpakis G (2015) Structure-activity relationships in the production of Olefins from alcohols and ethers: a first-principles theoretical study. Catal Sci Technol 4:4547–4555. https://doi.org/10.1039/c5cy00925a
33. Macht J, Janik MJ, Neurock M, Iglesia E (2008) Mechanistic consequences of composition in acid catalysis by polyoxometalate keggin clusters. J Am Chem Soc 130:10369–10379. https://doi.org/10.1021/ja803114r
34. Carr RT, Neurock M, Iglesia E (2011) Catalytic consequences of acid strength in the conversion of methanol to dimethyl ether. J Catal 278:78–93. https://doi.org/10.1016/j.jcat.2010.11.017
35. Macht J, Carr RT, Iglesia E (2009) Consequences of acid strength for isomerization and elimination catalysis on solid acids. J Am Chem Soc 131:6554–6565. https://doi.org/10.1021/ja900829x
36. Macht J, Carr RT, Iglesia E (2009) Functional assessment of the strength of solid acid catalysts. J Catal 264:54–66. https://doi.org/10.1016/j.jcat.2009.03.005
37. Sharifvaghefi S, Yang B, Zheng Y (2018) New insights on the role of H_2S and sulfur vacancies on Dibenzothiophene hydrodesulfurization over MoS_2 edges. Appl Catal A 566:164–173. https://doi.org/10.1016/j.apcata.2018.05.033
38. Wang H, Iglesia E (2010) Thiophene hydrodesulfurization catalysis on supported Ru clusters: mechanism and site requirements for hydrogenation and desulfurization pathways. J Catal 273:245–256. https://doi.org/10.1016/j.jcat.2010.05.019
39. Moses PG, Hinnemann B, Topsøe H, Nørskov JK (2009) The effect of Co-promotion on MoS_2 catalysts for hydrodesulfurization of Thiophene: a density functional study. J Catal 268:201–208. https://doi.org/10.1016/j.jcat.2009.09.016
40. Ding S, Jiang S, Zhou Y et al (2017) Catalytic characteristics of active corner sites in CoMoS nanostructure hydrodesulfurization–a mechanism study based on DFT calculations. J Catal 345:24–38. https://doi.org/10.1016/j.jcat.2016.11.011
41. Paul JF, Payen E (2003) Vacancy formation on MoS_2 hydrodesulfurization catalyst: DFT study of the mechanism. J Phys Chem B 107:4057–4064. https://doi.org/10.1021/jp027668f
42. Rangarajan S, Mavrikakis M (2016) DFT Insights into the competitive adsorption of sulfur- and nitrogen-containing compounds

and hydrocarbons on co-promoted molybdenum sulfide catalysts. ACS Catal 6:2904–2917. https://doi.org/10.1021/acscatal.6b00058
43. Baertsch CD, Komala KT, Chua YH, Iglesia E (2002) Genesis of brønsted acid sites during dehydration of 2-butanol on tungsten oxide catalysts. J Catal 205:44–57. https://doi.org/10.1006/JCAT.2001.3426
44. Fu J, Liu S, Zheng W et al (2022) Modulating the dynamics of Brønsted acid sites on $PtWO_x$ inverse catalyst. Nat Catal 5:144–153. https://doi.org/10.1038/s41929-022-00745-y
45. Greiner MT, Chai L, Helander MG et al (2012) Transition metal oxide work functions: the influence of cation oxidation state and oxygen vacancies. Adv Func Mater 22:4557–4568. https://doi.org/10.1002/adfm.201200615
46. Faye J, Capron M, Takahashi A et al (2015) Effect of oxomolybdate species dispersion on direct methanol oxidation to dimethoxymethane over MoO_x/TiO_2 catalysts. Energy Sci Eng 3:115–125. https://doi.org/10.1002/ese3.53
47. Liu H, Iglesia E (2003) Selective one-step synthesis of dimethoxymethane via methanol or dimethyl ether oxidation on $H_{3+n}V_nMo_{12-n}PO_{40}$ keggin structures. J Phys Chem B 107:10840–10847. https://doi.org/10.1021/JP0301554
48. Deshlahra P, Iglesia E (2014) Methanol oxidative dehydrogenation on oxide catalysts: molecular and dissociative routes and hydrogen addition energies as descriptors of reactivity. J Phys Chem C 118:26115–26129. https://doi.org/10.1021/jp507922u
49. Tatibouët J-M, Lauron-Pernot H (2001) Transient isotopic study of methanol oxidation on unsupported V_2O_5 mechanism of methylal formation. J Mol Catal A: Chem 171:205–216. https://doi.org/10.1016/S1381-1169(01)00104-2
50. Ai M (1983) The reaction of formaldehyde on various metal oxide catalysts. J Catal 83:141–150. https://doi.org/10.1016/0021-9517(83)90037-4
51. Ai M (1982) The production of methyl formate by the vapor-phase oxidation of methanol. J Catal 77:279–288. https://doi.org/10.1016/0021-9517(82)90168-3
52. KaichevPopova GYa, Chesalov YuA VV et al (2014) Selective oxidation of methanol to form dimethoxymethane and methyl formate over a monolayer V_2O_5/TiO_2 catalyst. J Catal 311:59–70. https://doi.org/10.1016/j.jcat.2013.10.026
53. Li H, Song H, Chen L, Xia C (2015) Designed SO_4^{2-}/Fe_2O_3-SiO_2 solid acids for polyoxymethylene dimethyl ethers synthesis: the acid sites control and reaction pathways. Appl Catal B 165:466–476. https://doi.org/10.1016/j.apcatb.2014.10.033
54. Peláez R, Marín P, Ordóñez S (2020) Synthesis of poly(oxymethylene) dimethyl ethers from methylal and trioxane over acidic ion exchange resins: a kinetic study. Chem Eng J 396:125305. https://doi.org/10.1016/j.cej.2020.125305
55. Grünert A, Losch P, Ochoa-Hernández C et al (2018) Gas-phase synthesis of oxymethylene ethers over Si-rich zeolites. Green Chem 20:4719–4728. https://doi.org/10.1039/c8gc02617c
56. Yao R, Herrera JE, Chen L, Chin YHC (2020) Generalized mechanistic framework for ethane dehydrogenation and oxidative dehydrogenation on molybdenum oxide catalysts. ACS Catal 10:6952–6968. https://doi.org/10.1021/acscatal.0c01073
57. Li N, Wang S, Ren Q et al (2016) Catalytic mechanisms of methanol oxidation to methyl formate on vanadia-titania and vanadia-titania-sulfate catalysts. J Phys Chem C 120:29290–29301. https://doi.org/10.1021/acs.jpcc.6b10289
58. Liu H, Iglesia E (2005) Selective oxidation of methanol and ethanol on supported ruthenium oxide clusters at low temperatures. J Phys Chem B 109:2155–2163. https://doi.org/10.1021/jp0401980
59. Pang Y, Ardagh MA, Shetty M et al (2021) On the spatial design of co-fed amines for selective dehydration of methyl lactate to acrylates. ACS Catal 11:5718–5735. https://doi.org/10.1021/acscatal.1c00573
60. Suarez W, Dumesic JA, Hill CG (1985) Acidic properties of molybdena-alumina for different extents of reduction: infrared and gravimetric studies of adsorbed pyridine. J Catal 94:408–421. https://doi.org/10.1016/0021-9517(85)90206-4
61. Herman GS, Dohnálek Z, Ruzycki N, Diebold U (2003) Experimental investigation of the interaction of water and methanol with anatase−TiO_2(101). J Phys Chem B 107:2788–2795. https://doi.org/10.1021/jp0275544
62. Foo GS, Hu G, Hood ZD et al (2017) Kinetics and mechanism of methanol conversion over anatase titania nanoshapes. ACS Catal 7:5345–5356. https://doi.org/10.1021/acscatal.7b01456
63. Wachs IE, Weckhuysen BM (1997) Structure and reactivity of surface vanadium oxide species on oxide supports. Appl Catal A 157:67–90. https://doi.org/10.1016/S0926-860X(97)00021-5
64. Centi G (1996) Nature of active layer in vanadium oxide supported on titanium oxide and control of its reactivity in the selective oxidation and ammoxidation of alkylaromatics. Appl Catal A 147:267–298. https://doi.org/10.1016/S0926-860X(96)00179-2
65. Machiels CJ, Sleight AW (1982) Kinetic isotope effect in the selective oxidation of methanol to formaldehyde over some molybdate catalysts. J Catal 76:238–239. https://doi.org/10.1016/0021-9517(82)90254-8
66. Kilos B, Bell AT, Iglesia E (2009) Mechanism and site requirements for ethanol oxidation on vanadium oxide domains. J Phys Chem C 113:2830–2836. https://doi.org/10.1021/jp8078056
67. Gong X, Ye Y, Chowdhury AD (2022) Evaluating the role of descriptor- and spectator-type reaction intermediates during the early phases of zeolite catalysis. ACS Catal 12:15463–15500. https://doi.org/10.1021/acscatal.2c04600
68. Bates JS, Biswas S, Suh S-E et al (2022) Chemical and electrochemical o_2 reduction on earth-abundant M–N–C catalysts and implications for mediated electrolysis. J Am Chem Soc 144:922–927. https://doi.org/10.1021/jacs.1c11126
69. Pomalaza G, Capron M, Ordomsky V, Dumeignil F (2016) Recent breakthroughs in the conversion of ethanol to butadiene. Catalysts 6:203. https://doi.org/10.3390/catal6120203
70. Lin F, Zhang J, Liu D, Chin Y-H, (Cathy), (2018) Cascade reactions in tunable lamellar micro- and mesopores for C=C bond coupling and hydrocarbon synthesis. Angew Chem 130:13068–13072. https://doi.org/10.1002/ange.201803929
71. Bayu A, Abudula A, Guan G (2019) Reaction pathways and selectivity in chemo-catalytic conversion of biomass-derived carbohydrates to high-value chemicals: a review. Fuel Process Technol 196:106162. https://doi.org/10.1016/j.fuproc.2019.106162
72. Bell RP (1936) The theory of reactions involving proton transfers. Proceedings Royal Soc of London Series A-Math Phys Sci 154:414–429. https://doi.org/10.1098/rspa.1936.0060
73. Evans MG, Polanyi M (1936) Further considerations on the thermodynamics of chemical equilibria and reaction rates. Trans Faraday Soc 32:1333. https://doi.org/10.1039/tf9363201333
74. Shangguan J, Chin Y-HC (2019) Kinetic significance of proton-electron transfer during condensed phase reduction of carbonyls on transition metal clusters. ACS Catal 9:1763–1778. https://doi.org/10.1021/acscatal.8b03470